

RH7

Determination of Feasible Return-to-Launchsite Aborts for an
HL-20 Personnel Launch System Vehicle Using Optimal
Control Theory

Kevin E. Dutton

B.A.E. December 1988, Rensselaer Polytechnic Institute

A Thesis submitted to

The Faculty of

The Graduate School of Engineering and Applied Science
of George Washington University in partial fulfillment
of requirements for the degree of Master of Science in Astronautics

July 6, 1993

Abstract

The Personnel Launch System (PLS) being studied by NASA is a system to complement the Space Shuttle and provide alternative access to space. The PLS consists of a manned spacecraft launched by an existing expendable launch vehicle (ELV) or a vehicle such as those proposed for the National Launch System program. A candidate for the manned spacecraft is the HL-20 lifting body.

In the event of an ELV malfunction during the initial portion of the ascent trajectory, the HL-20 will separate from the rocket and perform an unpowered return-to-launchsite (RTL) abort. This work details an investigation of the RTL abort scenario using optimal control theory. The objective of the abort trajectory is to maximize final altitude. With this selection of cost function, the feasibility of an RTL at different times along the ascent trajectory will be determined. The method of differential inclusions, which allows the determination of optimal states and eliminates the need for determining the optimal controls, is used to determine the optimal trajectories.

Acknowledgements

Several people in the Spacecraft Controls Branch (SCB) and outside of the branch contributed a great deal to this work. My thesis advisor, Dr. Robert Bless, applied the pressure which finally resulted in the work detailed in this report. Dr. Hans Seywald, also of SCB, is responsible for the development of the solution method used to solve the problem described in this work. His explanation of the method, associated code, and the mysterious hodograph in general were crucial. Chris Naftel, of the Vehicle Analysis Branch, was instrumental in providing HL-20 vehicle data, comparison cases, and miscellaneous important information without which the problem would have been much more difficult. Bruce Jackson, of the Aircraft Guidance and Control Branch, and Al Ragsdale, of UNISYS, introduced me to the HL-20 and the world of simulation. Finally, a thanks to the management of SCB and my co-workers who may not have contributed directly, but helped nonetheless.

Contents

Abstract	i
Acknowledgements	ii
Table of Contents	iii
List of Tables	v
List of Figures	vi
Nomenclature	ix
1 Introduction	1
1.1 Description of Abort Scenarios	1
1.2 Optimal Control Theory	2
1.3 Purpose of Work	2
2 Vehicle and Model Description	4
2.1 Vehicle Description	4
2.2 Aerodynamics	4
2.3 Atmospheric and Gravitational Model	6
2.4 Dynamic Model	6
3 Hodograph Analysis and Solution Method	9
3.1 Optimal Control Theory	9
3.2 The Hodograph and Set of Attainability	10
3.3 Numerical Approach	11

3.4	HL-20 RTLS Abort – Hodograph Analysis	12
4	Nominal Abort Case	17
4.1	Ascent Launch Profile	17
4.2	Separation Mechanism	17
4.3	Results for Abort at Thirty Seconds	18
4.3.1	Initial and Final Boundary Conditions	18
4.3.2	Nominal RTLS Case	19
4.3.3	Effect of Lift Coefficient Constraint	21
4.3.4	Effect of Freeing Final Conditions	21
4.3.5	Effect of Final Energy as Cost Function	22
5	Additional Abort Case Studies	23
6	Summary	26
	Bibliography	28

List of Tables

1	HL-20 Physical Parameters	30
2	Maximum Trim α and C_L	30
3	Coefficients for C_D expression	31
4	Parameters for Atmospheric and Gravitational Models	31
5	Comparison of Trajectory Conditions and Abort Initial Conditions at 30 Seconds	32
6	RTLS Abort Final Boundary Conditions	32
7	Initial Conditions for RTLS Aborts	32
8	Initial Conditions for RTLS Aborts	33

List of Figures

1	HL-20 Lifting Body	34
2	KSC Runway and Launch Pad Locations	35
3	Basic HL-20 Vehicle Drag Coefficient	35
4	Basic HL-20 Vehicle Lift Coefficient	36
5	Minimum and Maximum Trim C_L	36
6	C_{D_0} - Zeroeth-Order Coefficient for C_D	37
7	C_{D_1} - First-Order Coefficient for C_D	37
8	C_{D_2} - Second-Order Coefficient for C_D	38
9	Drag Polar (Two-Dimensional Hodograph)	38
10	Rotated Drag Polar (Three-Dimensional Hodograph)	39
11	Altitude vs. Time for Nominal Titan III/HL-20 Launch	39
12	Velocity vs. Time for Nominal Titan III/HL-20 Launch	40
13	Mach Number vs. Time for Nominal Titan III/HL-20 Launch	40
14	Latitude vs. Time for Nominal Titan III/HL-20 Launch	41
15	Longitude vs. Time for Nominal Titan III/HL-20 Launch	41
16	Flight Path Angle vs. Time for Nominal Titan III/HL-20 Launch	42
17	Azimuth vs. Time for Nominal Titan III/HL-20 Launch	42
18	Altitude vs. Time for Nominal RTLS Abort at 30 Seconds	43
19	Groundtrack for Nominal RTLS Abort at 30 Seconds	43
20	Velocity vs. Time for Nominal RTLS Abort at 30 Seconds	44
21	Flight Path Angle vs. Time for Nominal RTLS Abort at 30 Seconds	44
22	Heading vs. Time for Nominal RTLS Abort at 30 Seconds	45
23	Mach Number vs. Time for Nominal RTLS Abort at 30 Seconds	45
24	Dynamic Pressure vs. Time for Nominal RTLS Abort at 30 Seconds	46

25	Normal Load Factor vs. Time for Nominal RTLS Abort at 30 Seconds . . .	46
26	Axial Load Factor vs. Time for Nominal RTLS Abort at 30 Seconds	47
27	Lift Coefficient vs. Time for Nominal RTLS Abort at 30 Seconds	47
28	Bank Angle vs. Time for Nominal RTLS Abort at 30 Seconds	48
29	Drag Coefficient vs. Time for Nominal RTLS Abort at 30 Seconds	48
30	Altitude vs. Time for RTLS Abort at 30 Seconds: Effect of C_L Constraint .	49
31	Groundtrack for RTLS Abort at 30 Seconds: Effect of C_L Constraint	49
32	Velocity vs. Time for RTLS Abort at 30 Seconds: Effect of C_L Constraint .	50
33	Flight Path Angle vs. Time for RTLS Abort at 30 Seconds: Effect of C_L Constraint	50
34	Heading vs. Time for RTLS Abort at 30 Seconds: Effect of C_L Constraint .	51
35	Lift Coefficient vs. Time for RTLS Abort at 30 Seconds: Effect of C_L Constraint	51
36	Bank Angle vs. Time for RTLS Abort at 30 Seconds: Effect of C_L Constraint	52
37	Altitude vs. Time for RTLS Abort at 30 Seconds: Effect of Free Final Boundary Conditions	52
38	Groundtrack for RTLS Abort at 30 Seconds: Effect of Free Final Boundary Conditions	53
39	Velocity vs. Time for RTLS Abort at 30 Seconds: Effect of Free Final Bound- ary Conditions	53
40	Flight Path Angle vs. Time for RTLS Abort at 30 Seconds: Effect of Free Final Boundary Conditions	54
41	Heading vs. Time for RTLS Abort at 30 Seconds: Effect of Free Final Bound- ary Conditions	54
42	Lift Coefficient vs. Time for RTLS Abort at 30 Seconds: Effect of Free Final Boundary Conditions	55
43	Bank Angle vs. Time for RTLS Abort at 30 Seconds: Effect of Free Final Boundary Conditions	55
44	Altitude vs. Time for RTLS Abort at 30 Seconds: Effect of Final Energy as Cost Function	56
45	Groundtrack for RTLS Abort. at 30 Seconds: Effect of Final Energy as Cost Function	56

46	Velocity vs. Time for RTLS Abort at 30 Seconds: Effect of Final Energy as Cost Function	57
47	Flight Path Angle vs. Time for RTLS Abort at 30 Seconds: Effect of Final Energy as Cost Function	57
48	Heading vs. Time for RTLS Abort at 30 Seconds: Effect of Final Energy as Cost Function	58
49	Energy vs. Time for RTLS Abort at 30 Seconds: Effect of Final Energy as Cost Function	58
50	Lift Coefficient vs. Time for RTLS Abort at 30 Seconds: Effect of Final Energy as Cost Function	59
51	Bank Angle vs. Time for RTLS Abort at 30 Seconds: Effect of Final Energy as Cost Function	59
52	Initial Altitude for HL-20 RTLS Abort	60
53	Initial X for HL-20 RTLS Abort	60
54	Initial Y for HL-20 RTLS Abort	61
55	Initial Velocity for HL-20 RTLS Abort	61
56	Initial Flight Path Angle for HL-20 RTLS Abort	62
57	Initial Heading for HL-20 RTLS Abort	62
58	Cost Function vs. Abort Time	63
59	Altitude vs. Time for 15-, 30-, and 65-Second Aborts	63
60	Groundtrack for 15-, 30-, and 65-Second Aborts	64
61	Velocity vs. Time for 15-, 30-, and 65-Second Aborts	64
62	Mach Number vs. Time for 15-, 30-, and 65-Second Aborts	65
63	Flight Path Angle vs. Time for 15-, 30-, and 65-Second Aborts	65
64	Heading vs. Time for 15-, 30-, and 65-Second Aborts	66
65	Energy vs. Time for 15-, 30-, and 65-Second Aborts	66
66	Dynamic Pressure vs. Time for 15-, 30-, and 65-Second Aborts	67
67	Normal Load Factor vs. Time for 15-, 30-, and 65-Second Aborts	67
68	Axial Load Factor vs. Time for 15-, 30-, and 65-Second Aborts	68
69	Lift Coefficient vs. Time for 15-, 30-, and 65-Second Aborts	68
70	Bank Angle vs. Time for 15-, 30-, and 65-Second Aborts	69

Nomenclature

Roman Symbols

a	speed of sound, ft/sec
a_0, a_1, a_2, a_3	coefficients for speed of sound polynomial
a_N, a_x	normal and axial load factors
b	wing span, ft
c, d	state equality and inequality constraints
\bar{c}	wing chord, ft
C_L	lift coefficient
C_D	drag coefficient
$C_{D_0}, C_{D_1}, C_{D_2}$	coefficients for drag coefficient polynomial
C_M	moment coefficient
D	drag force, lb
E	vehicle energy per unit mass, (ft/sec) ²
f	dynamical equations
g, h	control equality and inequality constraints
g	magnitude of gravitational acceleration, ft/sec ²
g_0	magnitude of gravitational acceleration at sea level, ft/sec ²
h	altitude, ft
J	cost function
K	set of attainability
L	lift force, lb
m	mass, slugs
M	Mach number
p, q	hodograph equality and inequality constraints
q	dynamic pressure, lb/ft ²
r	distance of HL-20 from center of Earth, ft
R_e	radius of Earth, ft
S	HL-20 wing area, ft ² ; hodograph

t	time, sec
u	control vector
V	velocity, ft/sec
W	empty weight, lb
W_{OMS}	OMS fuel weight, lb
x	state vector; flat Earth downrange measurement, ft
x_{cg}	center of gravity location
x_{ref}	moment reference center
y	flat Earth crossrange measurement,ft

Greek Symbols

α	angle of attack, deg
β	density scale height, ft ⁻¹
δ	control surface deflection, deg.
Δ	aerodynamic coefficient increment due to control surface deflection
γ	flight path angle, deg
ρ	density, slugs/ft ³
ρ_0	sea level density, slugs/ft ³
σ	bank angle, deg
θ	longitude, deg
ϕ	cost function; latitude, deg
ψ	heading angle, deg
Ψ	boundary conditions
Ω	set of admissible controls

Subscripts

e	wing flaps
f	final time
l	lower body flaps

T	total aerodynamic quantity
u	upper body flaps
V	basic vehicle (control surfaces undeflected)
0	initial time

Acronyms

ATO	Abort-To-Orbit
CCAFS	Cape Canaveral Air Force Station
ELV	Expendable Launch Vehicle
KSC	Kennedy Space Center
OMS	Orbital Maneuvering System
PLS	Personnel Launch System
POST	Program to Optimize Simulated Trajectories
RTLS	Return-To-LaunchSite
SRM	Solid Rocket Motor
TAL	Transatlantic-Abort-Landing

Chapter 1

Introduction

The NASA Langley Research Center is currently studying a next generation of manned access to orbit vehicles. This system is known as the Personnel Launch System (PLS). One design under consideration is a lifting body vehicle attached to a current expendable launch vehicle (ELV) such as the Titan III or a future launch vehicle such as those proposed under the National Launch System program. This lifting body is known as the HL-20 and is shown in Figure 1. It is similar to previous lifting body vehicles that NASA has studied such as the Martin X-24A and the Northrop M2-F2 [1].

An HL-20 mission will begin with a vertical launch into orbit. It is assumed that the launch site is the Kennedy Space Center (KSC) at Cape Canaveral, Florida. Once in orbit, the HL-20 will carry out its primary duties such as Space Station Freedom crew transfer or satellite repair. When returning to Earth, the vehicle will reenter the atmosphere and glide to a horizontal landing in a manner similar to the Space Shuttle Orbiter.

1.1 Description of Abort Scenarios

An area of concern for the HL-20 mission is that of aborts along the ascent trajectory. Five abort modes were investigated in [2] and [3]. These are (1) on-the-pad, (2) return-to-launchsite (RTL), (3) ocean-landing-by-parachute, (4) transatlantic-abort-landing (TAL), and (5) abort-to-orbit (ATO). A description of these abort scenarios follows.

On-the-pad aborts would occur when the HL-20 is sitting on top of the ELV at Pad 40 at KSC and a problem occurs which necessitates that the crew be placed a safe distance

from the rocket in a short period of time. This abort would begin by firing a solid rocket motor (SRM) to remove the HL-20 from the rocket and then gliding the HL-20 to the Cape Canaveral Air Force Station (CCAFS) skid strip or the KSC Shuttle Landing Facility for a horizontal landing.

Immediately after launch and until 20 seconds, the vehicle could perform an RTLS abort to the Shuttle Landing Facility. Between 20 and 64 seconds the vehicle could glide back to the CCAFS skid strip. The skid strip abort is the RTLS abort that will be examined in detail in this paper. Figure 2 shows the locations of Pad 40, the skid strip and the Shuttle Landing Facility at KSC.

Between 65 and 430 seconds the vehicle would have to parachute to an ocean landing. Beginning at 430 seconds the vehicle could make a TAL at one of the sites which the Space Shuttle Orbiter currently uses as emergency landing sites. An ATO would be chosen from 490 to 510 seconds.

1.2 Optimal Control Theory

The problem of determining the feasibility of an RTLS abort at some time along the Titan III/HL-20 ascent is essentially that of an aerospace vehicle performing a minimum energy glide and turn through the atmosphere to a runway, meeting some final boundary conditions and satisfying some state and control equality and inequality constraints. Optimal control theory has been applied to the problem of hypersonic glide in [4]. Chern and Vinh considered the problem of maximum downrange and other cost functions for both flat Earth and spherical Earth models. Their analysis investigated the optimal control problem using the calculus of variations approach to derive the first-order necessary conditions for optimality described in [5]. For each problem considered, the assumption of constant Mach number was made in [4]. Much of the work dealt with 2-dimensional cases; the 3-dimensional cases investigated were maximum crossrange and footprint calculation.

1.3 Purpose of Work

The use of optimal control theory applied to an RTLS problem could determine the ultimate RTLS performance of the HL-20, whereas the application of a simulation tool with less

Chapter 5

Additional Abort Case Studies

The initial conditions for aborts beginning at times from 15 to 65 seconds along the launch trajectory are given in Tables 7 and 8 and also in Figures 52–57. As stated previously, the initial conditions used for the RTLS abort at time T are the conditions at time T in the ascent, followed by a primary SRM burn and then a sustainer SRM burn. The sustainer SRM burn is not used for the 60 and 65 second cases because the vehicle was unable to return to the skid strip after it was fired.

The final conditions for all cases are the same as the final conditions for the 30 second case described previously. They are $x(t_f) = y(t_f) = 0$ ft, $V(t_f) = 520.8$ ft/sec, $\gamma(t_f) = -19.0^\circ$, and $\psi(t_f) = -220.7^\circ$.

It was found that the vehicle could make it back to the skid strip between 15 seconds and 65 seconds into the launch. No data was available for the time before 15 seconds. After 65 seconds, the vehicle is too far from the skid strip to return and would land in the ocean by deploying a parachute.

The cost function (final altitude) is shown in Figure 58 plotted against the time along the launch trajectory at which an abort procedure is initiated. It is seen that the final altitude in all cases is greater than the critical altitude of 2000 feet, which is necessary for an abort to be possible.

The 15, 30, and 65 second cases are now examined in detail. Figures 59–70 show the states and controls for RTLS aborts at these times.

Figure 59 shows that the final altitudes were 11200 ft, 17700 ft, and 11300 ft for the 15, 30, and 65 second abort cases, respectively. Making the same assumptions for the 15

and 65 second abort cases as were made for the 30 second case in the previous chapter, it is seen that there is some altitude margin at the final point, and an RTLS abort is possible at 15 and 65 seconds into the launch.

Each abort case exhibits the same characteristic of trading velocity for altitude to reach some maximum altitude, and then continually losing altitude for the rest of the trajectory (Figure 59). This was mentioned in the previous chapter for the 30 second abort case. It can be seen that the initial altitude increases as the launch time increases from 15 to 30 to 65 seconds as the ELV/HL-20 climbs on its ascent trajectory. The 65 second case is seen to have a much longer time of flight than the other two cases (280 seconds compared to 120 seconds).

The groundtrack of the three cases shows the eastward travel of the ELV as it ascends from 15 to 30 to 65 seconds, and also shows that the 65 second case has a much longer groundtrack than the other two cases (Figure 60), as would be expected from the much longer time of flight. All cases end up at the origin of the coordinate system heading in a northwesterly direction as desired.

The velocity and Mach number profiles in Figures 61 and 62 show that initial velocity and Mach number increase as the launch time increases from 15 to 30 to 65 seconds. They also show that for each case the velocity initially decreases as the vehicle climbs, and that after it reaches its maximum altitude the vehicle picks up speed as it dives. In the 65 second abort case, the vehicle starts supersonic, becomes subsonic during its climb and then becomes supersonic again during the dive and finally ends at a subsonic velocity. The final velocity in each case is the desired $V(t_f) = 520.8$ ft/sec.

The characteristics of climbing and losing speed and diving and gaining speed can also be seen in the flight path angle histories (Figure 63), which also shows that the ascent trajectory is flattening out (decreasing $\gamma(t_0)$) as the ELV climbs from 30 to 65 seconds. Oscillations are apparent in the flight path angle history, and in the 65 second case the vehicle reaches a maximum negative γ of nearly -80° . The final flight path angle in each case is the desired $\gamma(t_f) = -19^\circ$.

The heading history for each case shows nearly easterly flight along the ascent trajectory and a final heading aligned with the runway. It is also seen that in each case the vehicle wants to turn to the right (decreasing ψ) for the entire duration of the trajectory, ending in each case at the desired $\psi(t_f) = -220.7^\circ$ (Figure 64).

The energy profiles (Figure 65) show that initial energy increases along the ascent trajectory and that final energy, with final velocity fixed, exhibits the same characteristic as final altitude for the three cases. That is, just as $h(t_f)$ for the 30 second abort case is greater than $h(t_f)$ for the 65 second case which is greater than $h(t_f)$ for the 15 second case, so is $E(t_f)$ for the 30 second case greater than $E(t_f)$ for the 65 second case which is greater than $E(t_f)$ for the 15 second case.

The plots of dynamic pressure q (Figure 66) show that q increases during the ascent from 30 to 65 seconds and that the maximum dynamic pressure, q_{max} , occurs in each case at the initial time, since velocity immediately decreases and altitude immediately increases, both conditions contributing to a lower q .

The normal and axial load factors, as defined in Eqs. 4.1 and 4.2, are shown in Figures 67 and 68. The load factors do not present a problem in the 15 and 30 second abort cases. During the 65 second case however, on the pullout from the $\gamma = -80$ degree dive, the load factors increase to 4.2 and 2.5 for the normal and axial, respectively. A constraint on the load factors could be imposed if these values were considered too large.

The reason for the high load factors can be seen from a plot of lift coefficient which has been backed out from the states and state rates (Figure 69). For the 65 second abort case, a spike in the C_L history occurs at the pullout of the dive, resulting directly in the normal load factor spike, and, indirectly through drag coefficient, resulting in the spike in the axial load factor spike.

Finally, backing out bank angle and displaying it for the three cases (Figure 70) it is seen that for the 15 and 30 second cases, inverted flight is desired ($\sigma < -90^\circ$) at the beginning of the trajectory with the remainder of the trajectory flying upright. For the 65 second case however, the vehicle begins upright, flies inverted for a time, and then ends upright with a significant portion of time spent flying with nearly 0° bank angle.

As stated previously, some altitude margin exists for the 15 and 65 second abort cases. Since data was not available for the time before 15 seconds, it is not known if an abort of this type is possible. The latest time an abort is possible would be slightly after 65 seconds (but before 70 seconds since an abort was not possible at this point due to the distance of the vehicle from the skid strip). At all the times for which initial conditions are given in the tables, RTLS aborts were also possible but the data is not shown here since the 15, 30, and 65 second cases are considered representative of all of the cases.

Chapter 6

Summary

This work has applied optimal control theory to an RTLS abort of the HL-20 vehicle carried into orbit by a Titan III ELV. The trajectories that resulted were not the trajectories the HL-20 would follow to return to the skid strip at CCAFS since the objective was to maximize the final altitude. Instead, the problem determined the feasibility of an RTLS abort at different times along the launch trajectory.

When applying optimal control theory to an RTLS abort problem, the choice of a cost function is not evident. When final altitude is selected as the quantity to maximize, the problem becomes one of determining the feasibility of an RTLS abort, and not the determination of the actual RTLS abort trajectory, which is also of interest to the trajectory designer.

It was found that for the HL-20 launched from KSC Pad 40, RTLS aborts could be performed to runway 31 of the KSC skid strip between the launch times of 15 seconds and 65 seconds, after which, though the vehicle energy has increased, the vehicle is too far away to glide back.

Maximizing final altitude with final velocity fixed is nearly the same problem as maximizing final energy (or minimizing energy loss). The minimum energy loss problem has application in the calculation of the maximum achievable ground coverage, or footprint, of a reentry vehicle or the abort paths of vehicles such as the National Aerospace Plane.

Additional future work in the area of optimal RTLS aborts could involve shaping the ascent trajectory of the Titan III/HL-20 to maximize the amount of time during which an RTLS abort could be performed. The use of the OMS engines during the abort phase

and adding guidance logic to the primary SRM and sustainer SRM burns could also be investigated.

Bibliography

- [1] Talay, Theodore A, and Stone, Howard A., "The Personnel Launch System - a Lifting Body Approach," IAF-91-202, October 1991.
- [2] Naftel, J.C., Powell, Richard W., and Talay, Theodore A., "Performance Assessment of a Space Station Rescue and Personnel/Logistics Vehicle," *Journal of Spacecraft and Rockets*, Vol.27, No. 1, January-February 1990, pp. 76-81.
- [3] Naftel, J.Chris, and Talay, Theodore A., "Ascent Abort Capability for the HL-20," *Journal of Spacecraft and Rockets*, to be published.
- [4] Chern, Jeng-Shing, and Vinh, Nguyen Xuan, "Optimum Reentry Trajectories of a Lifting Vehicle," NASA Contractor Report 3236, February 1980.
- [5] Bryson, Arthur E., and Ho, Yu-Chi, *Applied Optimal Control - Optimization, Estimation, and Control*, Hemisphere Publishing Corporation, New York, NY, 1975.
- [6] Brauer, G.L., Cornick, D.E., and Stevenson, R., "Capabilities and Applications of the Program to Optimize Simulated Trajectories (POST)," NASA CR-2770, 1977.
- [7] Jackson, E. Bruce , and Cruz, Christopher I., "Real-Time Simulation Model of the HL-20 Lifting Body," NASA TM 107580, July 1992.
- [8] Committee on Extension to the Standard Atmosphere (COESA), *U.S. Standard Atmosphere, 1962*, Government Printing Office, Washington, D.C., 1962.
- [9] Seywald, Hans, "Trajectory Optimization Based on Differential Inclusion," NASA Contractor Report 4501, February 1993.

- [10] Gill, Philip E., Murray, Walter, Saunders, Michael A., and Wright, Margaret H., "User's Guide for NPSOL (Version 4.0): a Fortran Package for Nonlinear Programming," Systems Optimization Laboratory, Department of Operations Research, Stanford University, January 1986.
- [11] Cliff, E.M., Seywald, H., and Bless, R., "Hodograph Analysis in Aircraft Trajectory Optimization," AIAA 93-3742, August 1993.

Table 1: HL-20 Physical Parameters

Chord length	\bar{c}	27.31 ft
Span	b	13.89 ft
Wing area	S	286.45 ft ²
Empty weight	W	22932 lbs
OMS fuel weight	W_{OMS}	2948 lbs
C.G. Location (empty)	x_{cg}	55.5%
C.G. location (full)	x_{cg}	57.5%

Table 2: Maximum Trim α and C_L

Mach Number	Max α_{trim} (deg)	Max $C_{L_{trim}}$	Min $C_{L_{trim}}$
0.3	16.0	0.6628	-0.2045
0.6	16.0	0.7009	-0.2340
0.8	16.0	0.7285	-0.2949
0.9	16.0	0.7487	-0.1950
0.95	16.0	0.7491	-0.3357
1.1	16.0	0.6574	-0.1906
1.2	16.0	0.6288	-0.2106
1.6	9.4	0.2537	-0.0838
2.0	10.6	0.2643	-0.0737
2.5	12.0	0.2477	-0.0658
3.0	16.0	0.3895	-0.0530
3.5	16.0	0.3592	-0.0489
4.0	16.0	0.3422	-0.0457

Table 3: Coefficients for C_D expression

Mach Number	C_{D_2}	C_{D_1}	C_{D_0}
0.3	0.3263	-0.0200	0.0438
0.6	0.3783	-0.0169	0.0473
0.8	0.4171	-0.0151	0.0491
0.9	0.5310	-0.1014	0.0788
0.95	0.4636	-0.0240	0.0756
1.1	0.7288	-0.1605	0.1640
1.2	0.6507	-0.0774	0.1534
1.6	0.8535	0.0098	0.1494
2.0	0.3606	0.0625	0.1410
2.5	0.6474	0.0266	0.1270
3.0	0.9923	-0.0499	0.1167
3.5	1.0738	-0.0325	0.1101
4.0	1.0992	-0.0121	0.1080

Table 4: Parameters for Atmospheric and Gravitational Models

ρ_0	2.3769e-03 slugs/ft ³
β	3.6000e-05 ft ⁻¹
a_0	1.1235e+03 ft/sec
a_1	-5.7923e-03 sec ⁻¹
a_2	6.2641e-08 ft ⁻¹ sec ⁻¹
a_3	-1.7708e-13 ft ⁻² sec ⁻¹
g_0	3.2174e+01 ft/sec ²
R_e	2.0926e+07 ft

Table 5: Comparison of Trajectory Conditions and Abort Initial Conditions at 30 Seconds

	Trajectory Conditions	Abort Initial Conditions
Altitude, ft	$1.07025576e + 04$	$2.77408551e + 04$
Velocity, ft/sec	$8.04746952e + 02$	$1.01506581e + 03$
Latitude, deg	$2.84006296e + 01$	$2.84001727e + 01$
Longitude, deg	$2.79428431e + 02$	$2.79445672e + 02$
Flight Path Angle, deg	$7.11376932e + 01$	$6.49159663e + 01$
Azimuth, deg	$9.16395039e + 01$	$9.19469374e + 01$

Table 6: RTLS Abort Final Boundary Conditions

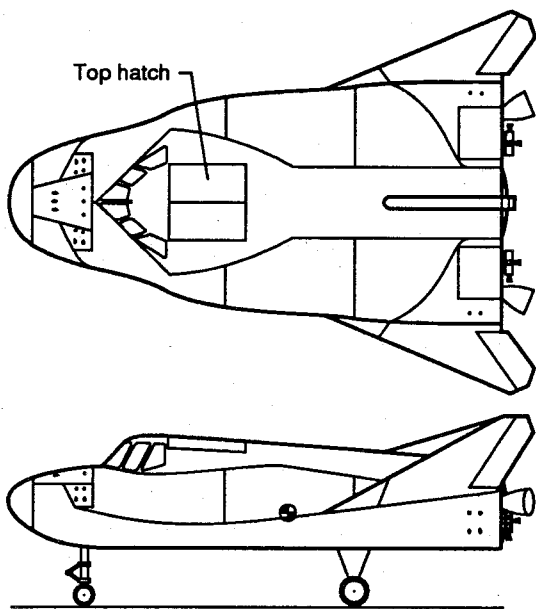
Downrange, ft	x	0
Crossrange, ft	y	0
Velocity, ft/sec	V	520.8
Flight Path Angle, deg	γ	-19.0
Heading, deg	ψ	-220.7

Table 7: Initial Conditions for RTLS Aborts

Time (sec)	h(ft)	x(ft)	y(ft)
15.0	$1.8745648e+04$	$-5.7470680e+03$	$4.5283500e+04$
20.0	$1.9542422e+04$	$-1.4644223e+04$	$4.5599964e+04$
25.0	$2.3134577e+04$	$-9.1229215e+03$	$4.5412128e+04$
30.0	$2.7740855e+04$	$-6.3246933e+03$	$4.5323737e+04$
35.0	$3.3599490e+04$	$-3.2577126e+03$	$4.5222760e+04$
40.0	$4.0475148e+04$	$6.3478304e+02$	$4.5090776e+04$
45.0	$4.7865123e+04$	$6.0726763e+03$	$4.4902247e+04$
50.0	$5.5686139e+04$	$1.2990810e+04$	$4.4656591e+04$
55.0	$6.4005911e+04$	$2.1276190e+04$	$4.4355667e+04$
60.0	$5.0263039e+04$	$1.2722135e+04$	$4.4203290e+04$
65.0	$5.8047153e+04$	$2.0051551e+04$	$4.4405061e+04$

Table 8: Initial Conditions for RTLS Aborts

Time (sec)	V (ft/sec)	γ (deg)	ψ (deg)
15.0	1.0011717e+03	5.2205378e+01	-1.9757279e+00
20.0	9.2742651e+02	7.8466266e+01	-1.8261807e+02
25.0	9.6635809e+02	6.9053372e+01	-1.9055671e+00
30.0	1.0150658e+03	6.4915966e+01	-1.9469374e+00
35.0	1.1221480e+03	6.5218080e+01	-1.9956142e+00
40.0	1.3057310e+03	6.5236462e+01	-2.0383687e+00
45.0	1.5278721e+03	6.2192217e+01	-2.0711914e+00
50.0	1.7782816e+03	5.7285346e+01	-2.1044202e+00
55.0	2.0602513e+03	5.2767337e+01	-2.1401928e+00
60.0	2.5275142e+03	5.3469427e+01	-3.0684166e+00
65.0	2.7780916e+03	5.0050729e+01	-2.0997439e+00



HL-20 Lifting Body

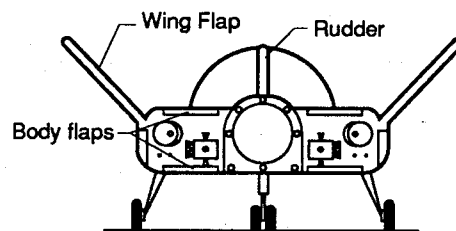


Figure 1: HL-20 Lifting Body

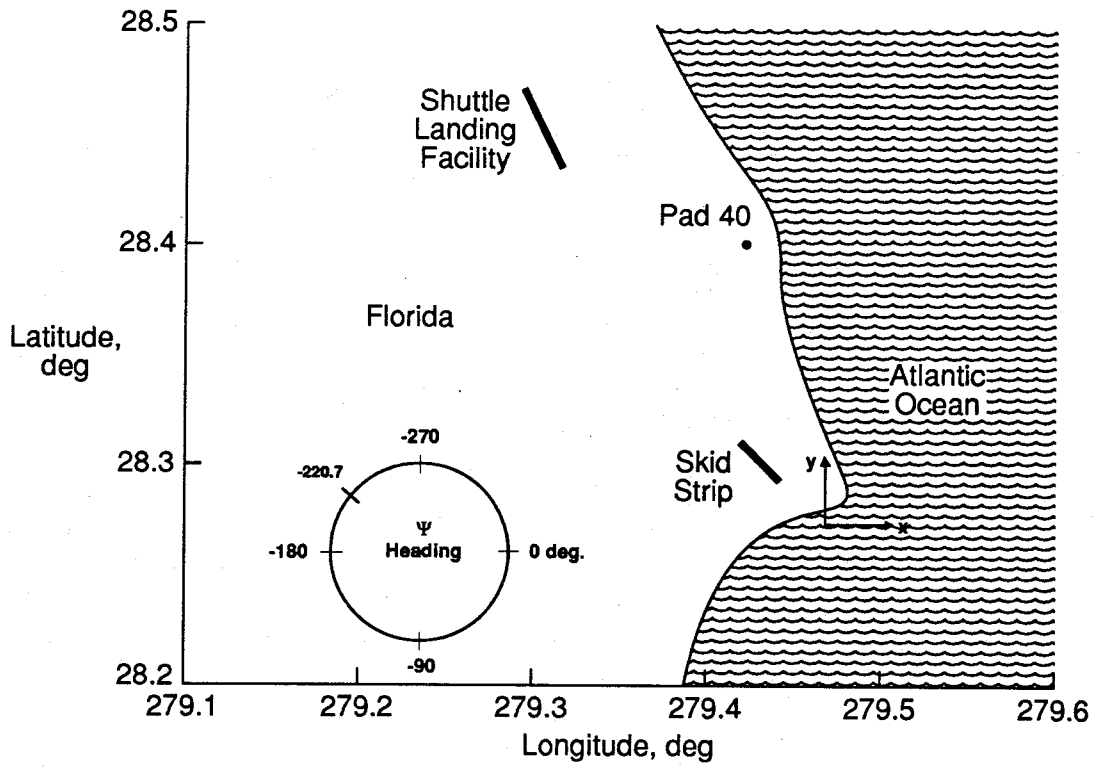


Figure 2: KSC Runway and Launch Pad Locations

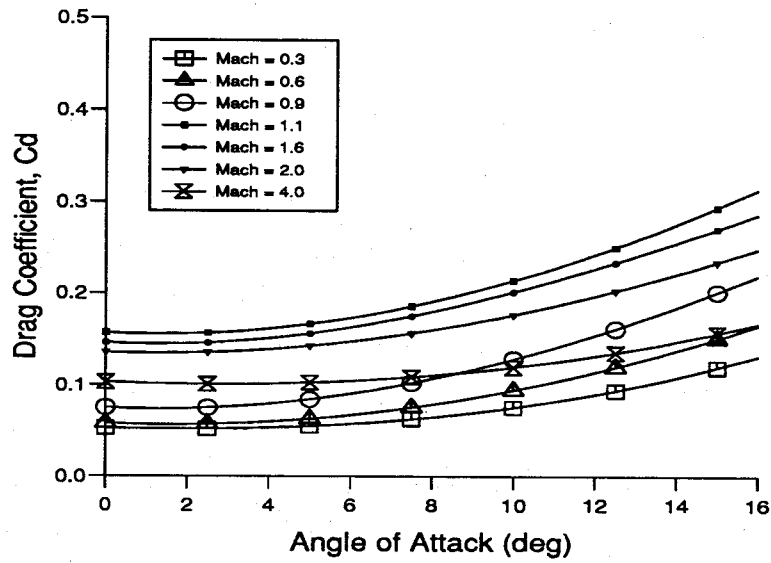


Figure 3: Basic HL-20 Vehicle Drag Coefficient

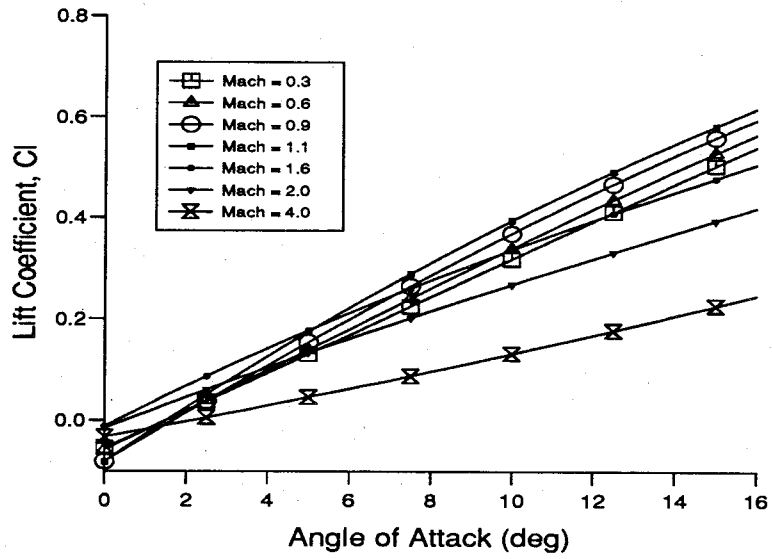


Figure 4: Basic HL-20 Vehicle Lift Coefficient

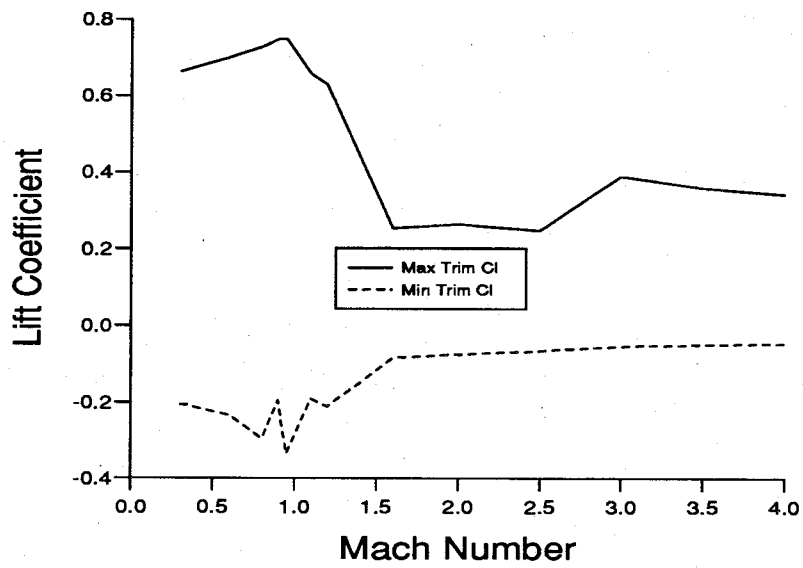


Figure 5: Minimum and Maximum Trim C_L

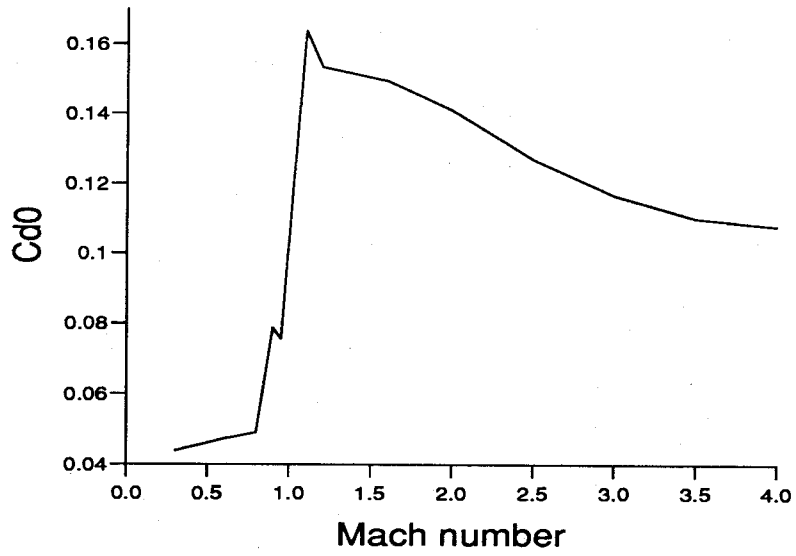


Figure 6: C_{D_0} - Zeroth-Order Coefficient for C_D

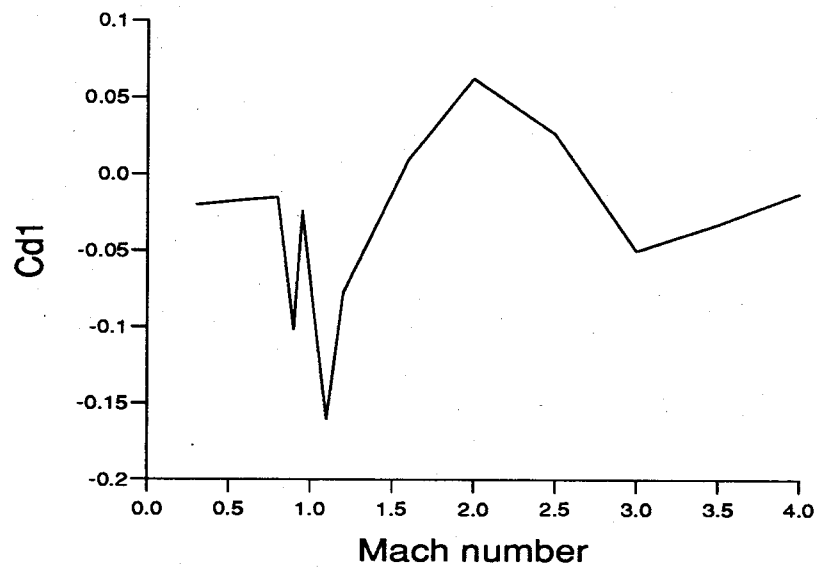


Figure 7: C_{D_1} - First-Order Coefficient for C_D

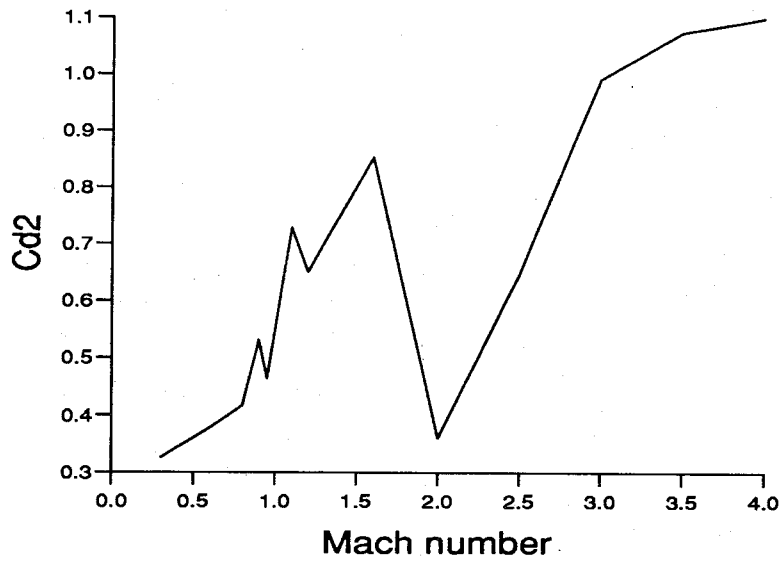


Figure 8: C_{D2} - Second-Order Coefficient for C_D

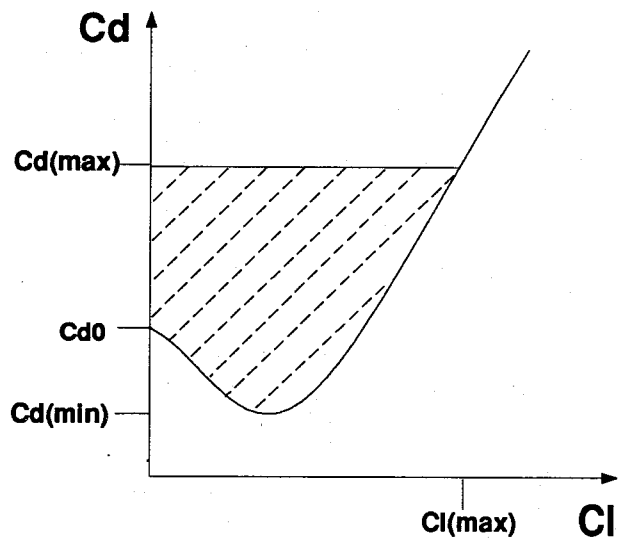


Figure 9: Drag Polar (Two-Dimensional Hodograph)

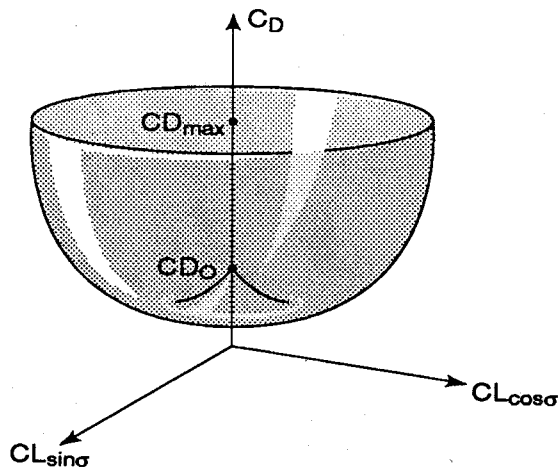


Figure 10: Rotated Drag Polar (Three-Dimensional Hodograph)

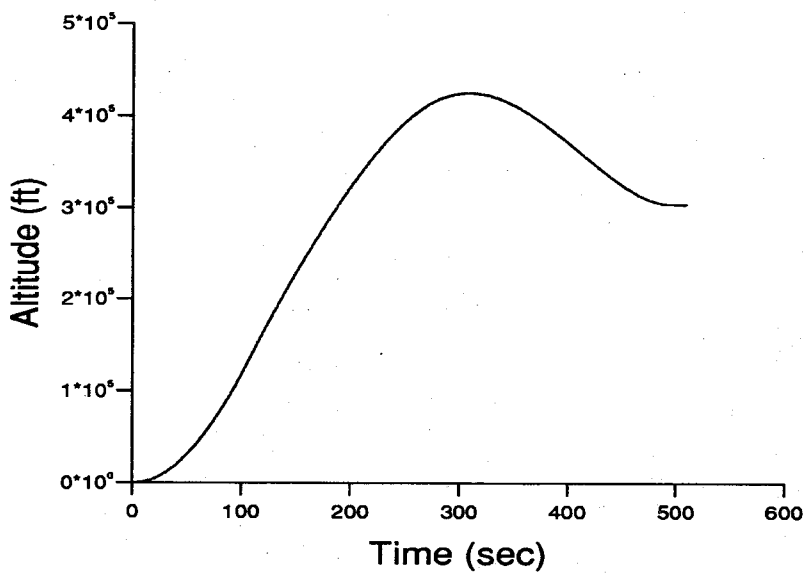


Figure 11: Altitude vs. Time for Nominal Titan III/HL-20 Launch

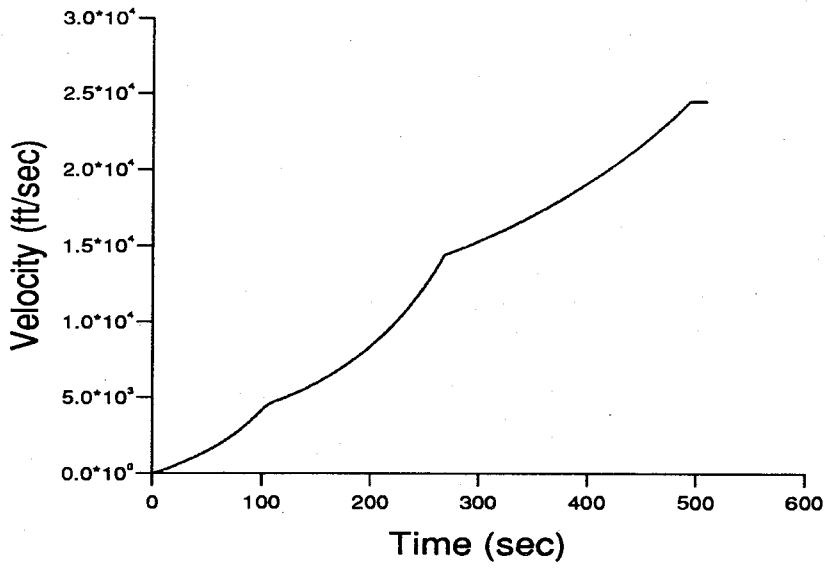


Figure 12: Velocity vs. Time for Nominal Titan III/HL-20 Launch

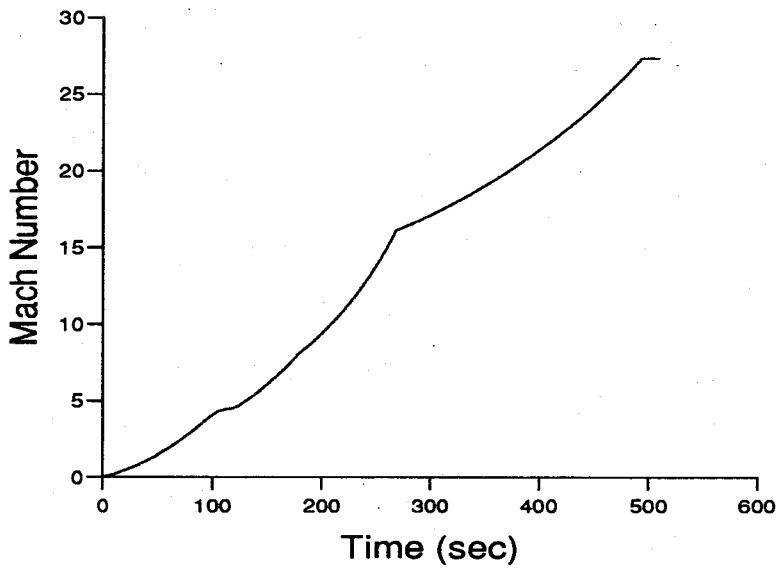


Figure 13: Mach Number vs. Time for Nominal Titan III/HL-20 Launch

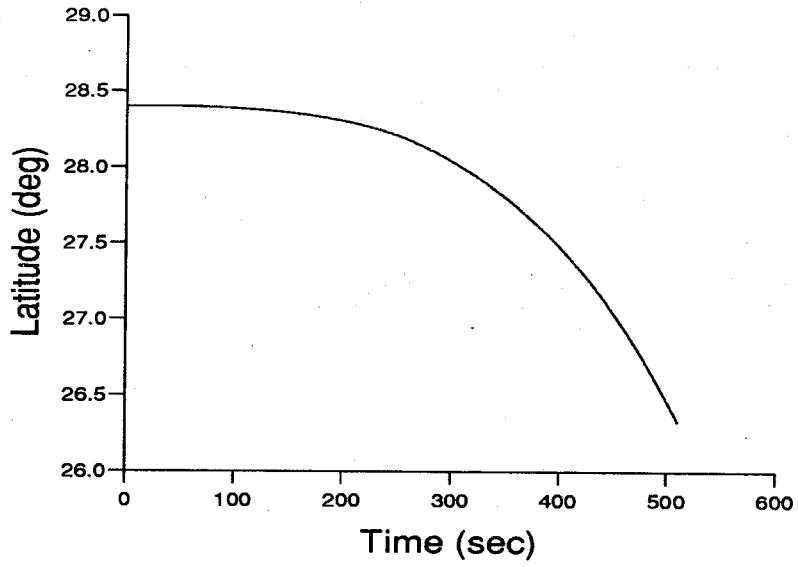


Figure 14: Latitude vs. Time for Nominal Titan III/HL-20 Launch

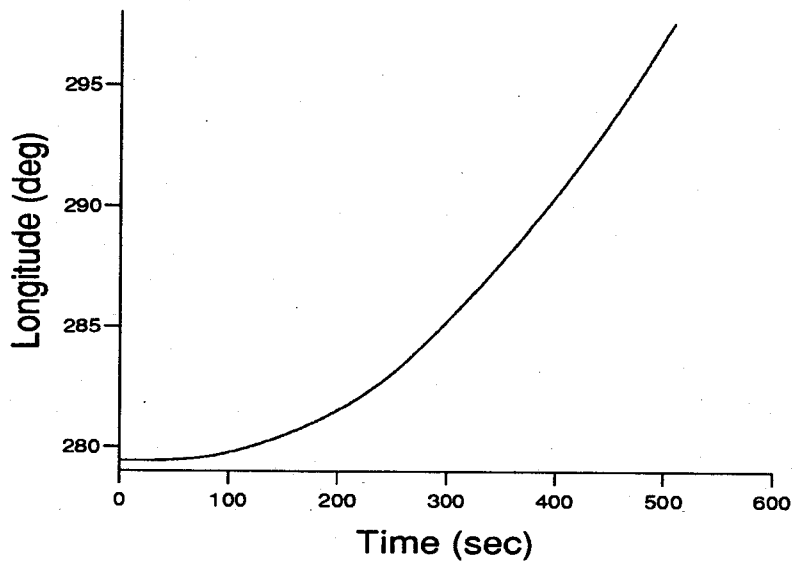


Figure 15: Longitude vs. Time for Nominal Titan III/HL-20 Launch

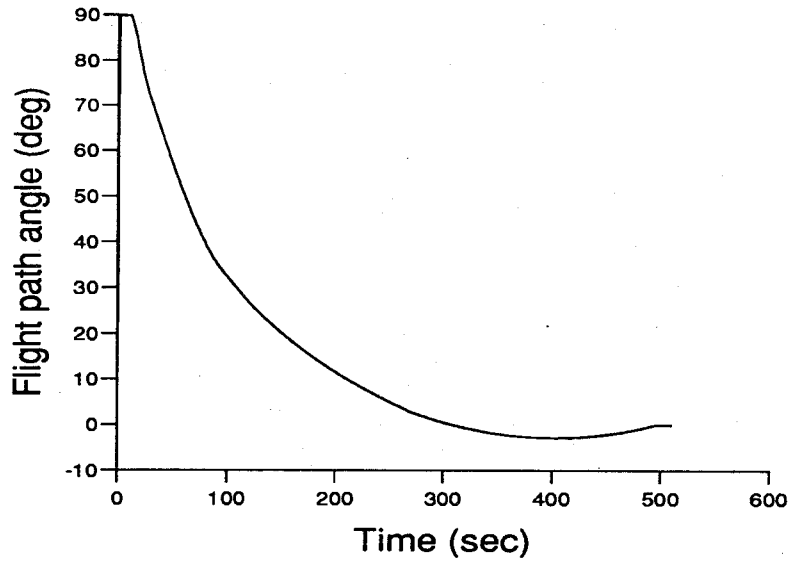


Figure 16: Flight Path Angle vs. Time for Nominal Titan III/HL-20 Launch

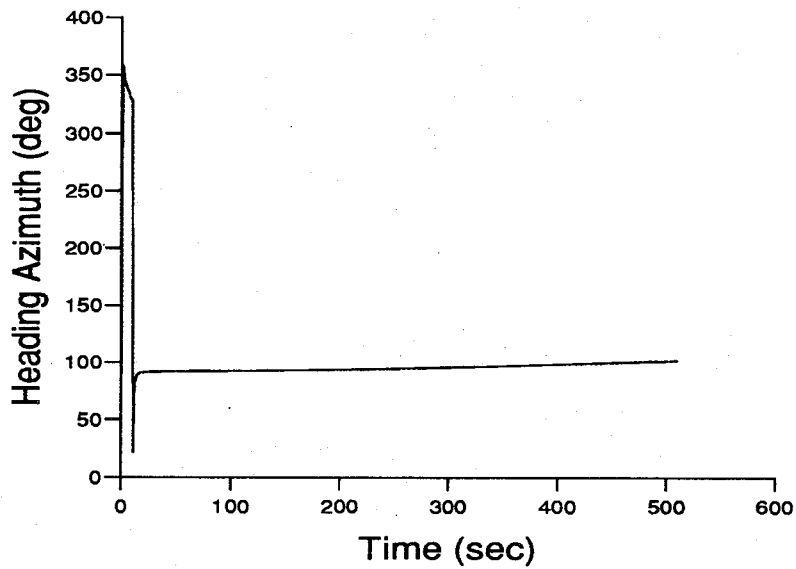


Figure 17: Azimuth vs. Time for Nominal Titan III/HL-20 Launch

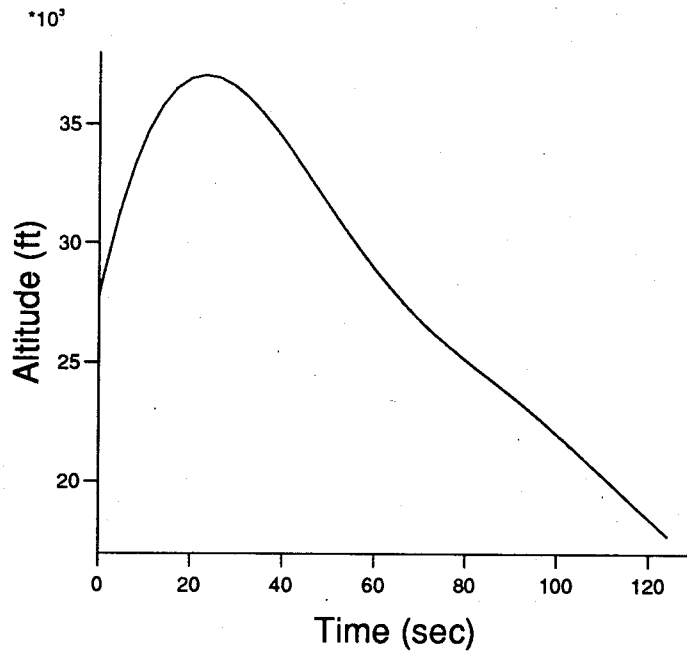


Figure 18: Altitude vs. Time for Nominal RTLS Abort at 30 Seconds

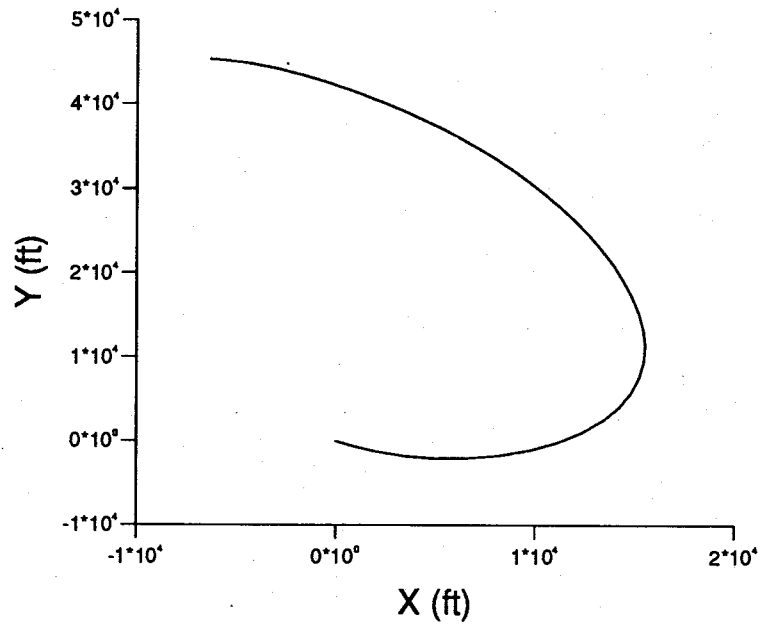


Figure 19: Groundtrack for Nominal RTLS Abort at 30 Seconds

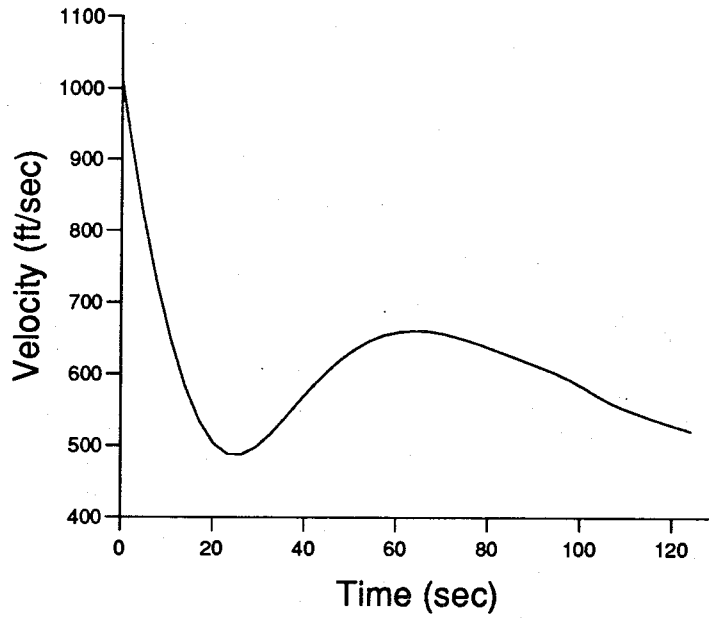


Figure 20: Velocity vs. Time for Nominal RTLS Abort at 30 Seconds

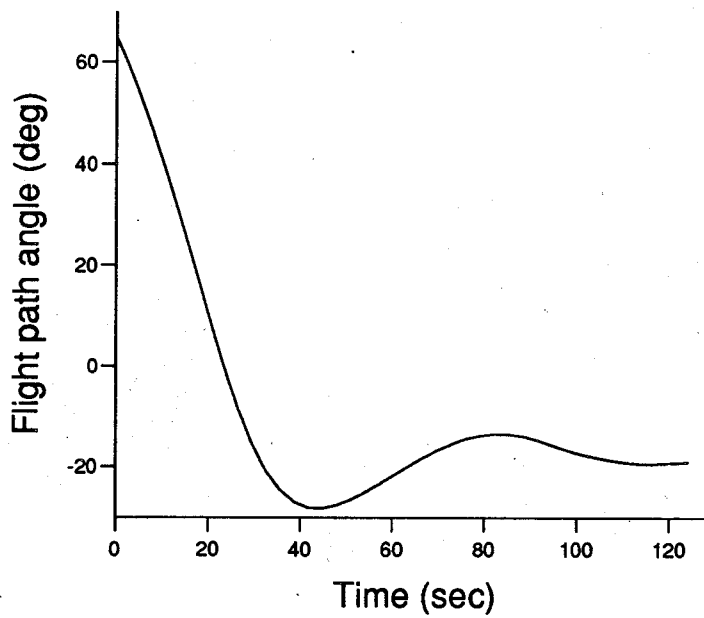


Figure 21: Flight Path Angle vs. Time for Nominal RTLS Abort at 30 Seconds

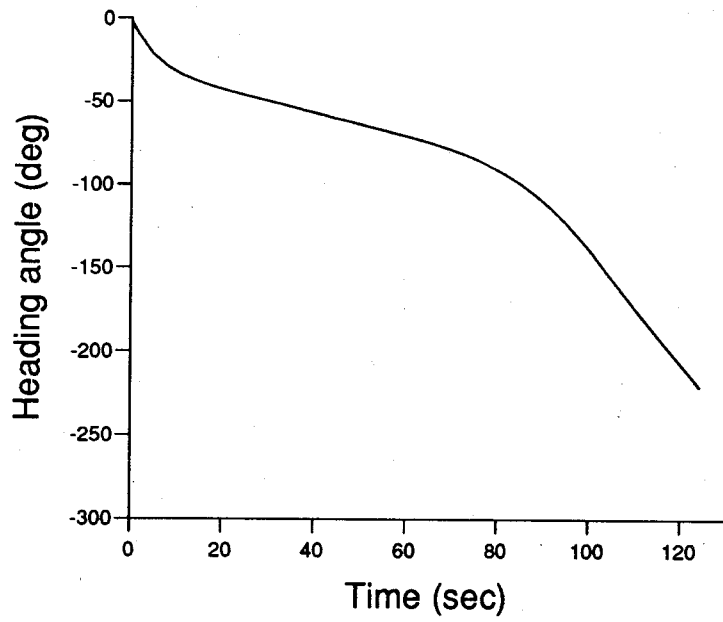


Figure 22: Heading vs. Time for Nominal RTLS Abort at 30 Seconds

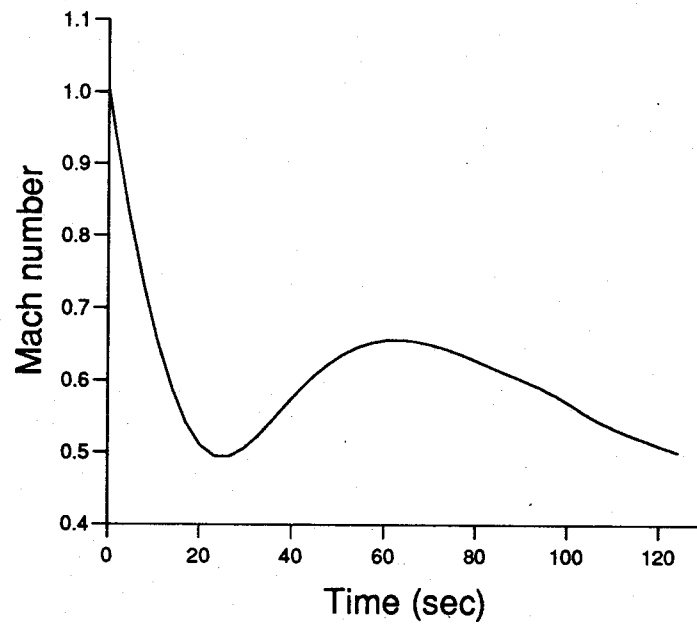


Figure 23: Mach Number vs. Time for Nominal RTLS Abort at 30 Seconds

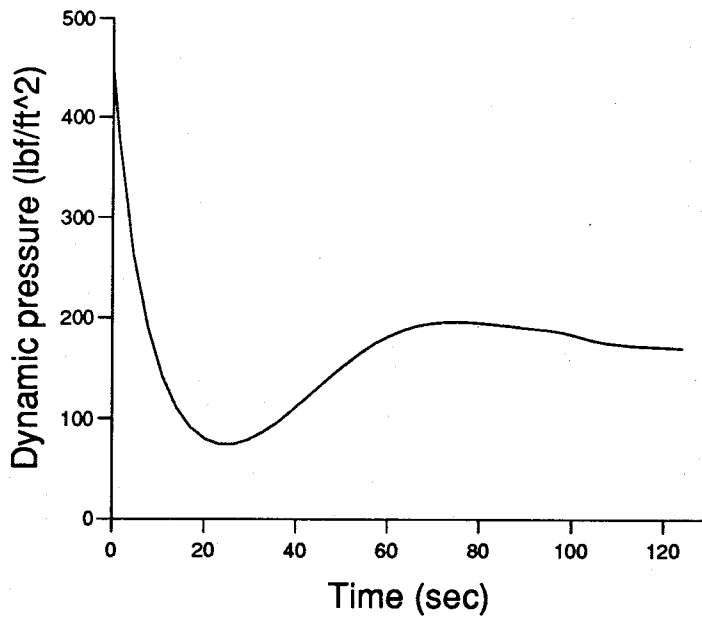


Figure 24: Dynamic Pressure vs. Time for Nominal RTLS Abort at 30 Seconds

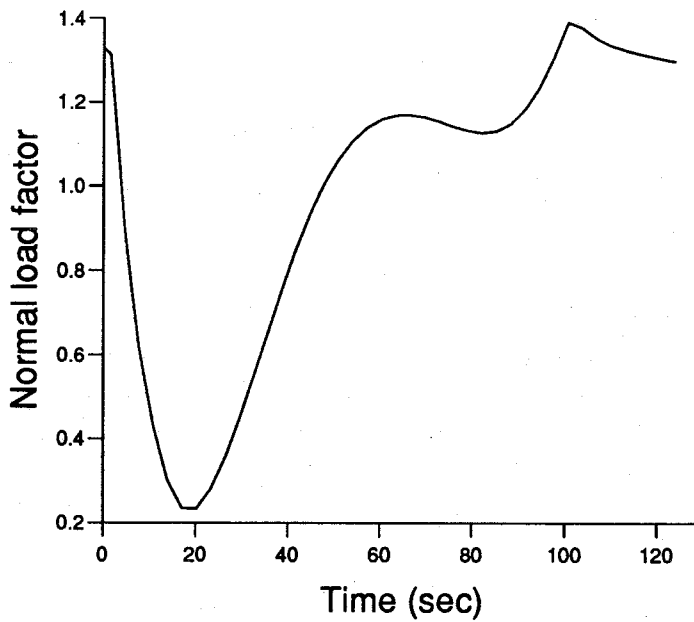


Figure 25: Normal Load Factor vs. Time for Nominal RTLS Abort at 30 Seconds

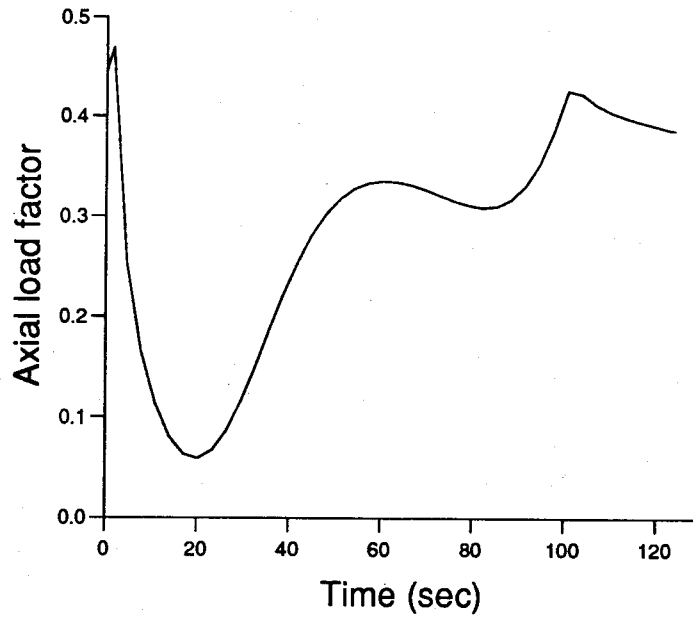


Figure 26: Axial Load Factor vs. Time for Nominal RTLS Abort at 30 Seconds

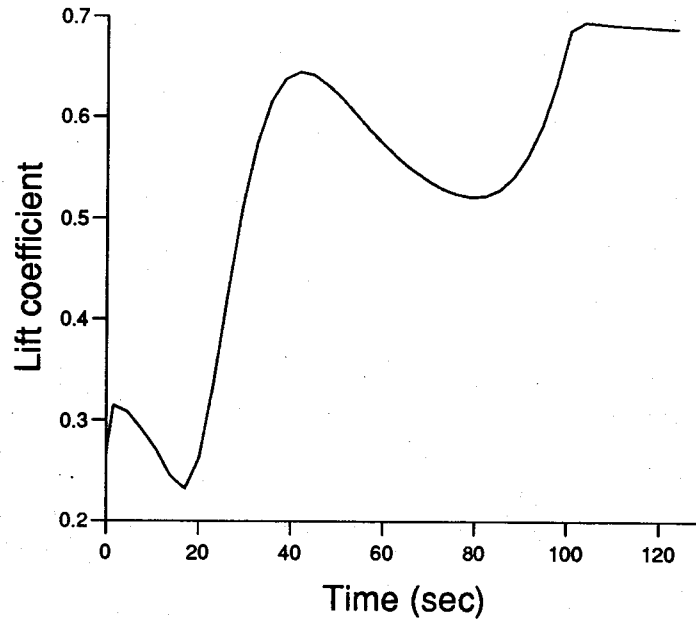


Figure 27: Lift Coefficient vs. Time for Nominal RTLS Abort at 30 Seconds

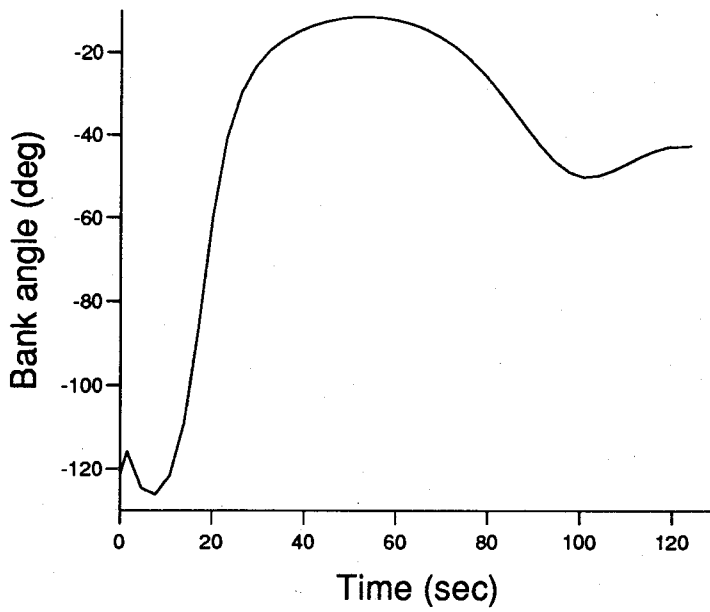


Figure 28: Bank Angle vs. Time for Nominal RTLS Abort at 30 Seconds

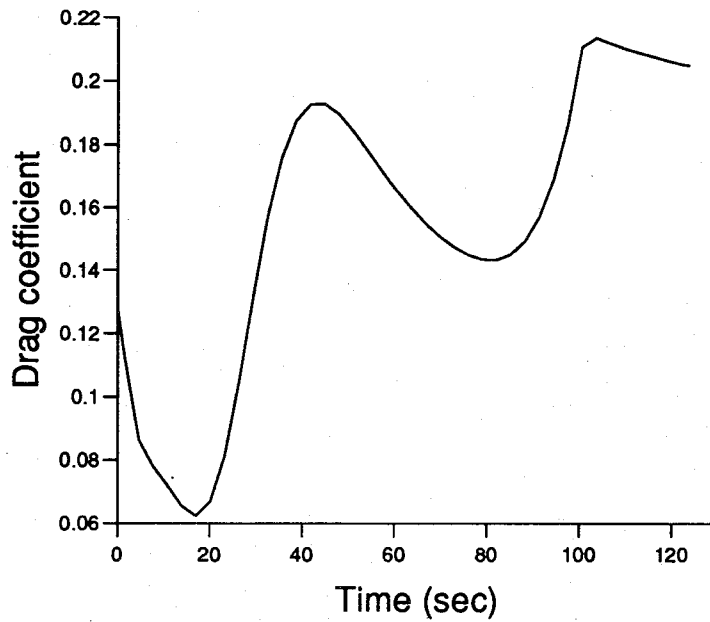


Figure 29: Drag Coefficient vs. Time for Nominal RTLS Abort at 30 Seconds

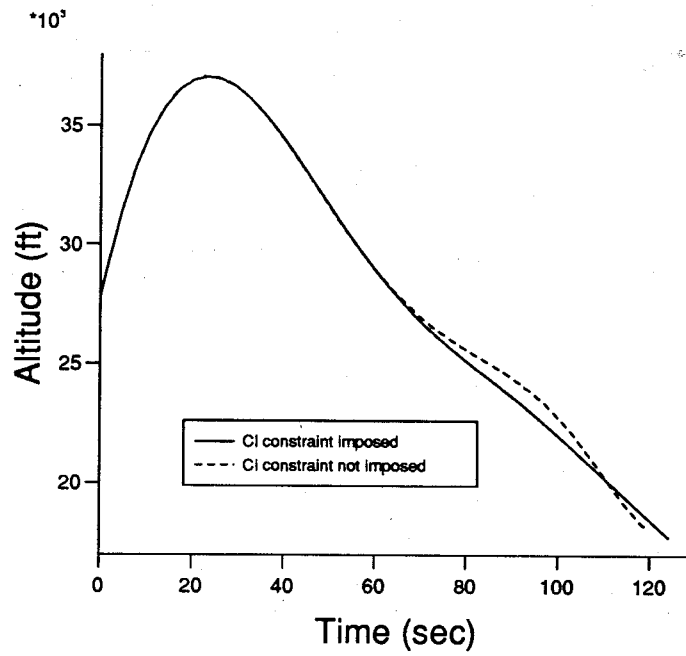


Figure 30: Altitude vs. Time for RTLS Abort at 30 Seconds: Effect of C_L Constraint

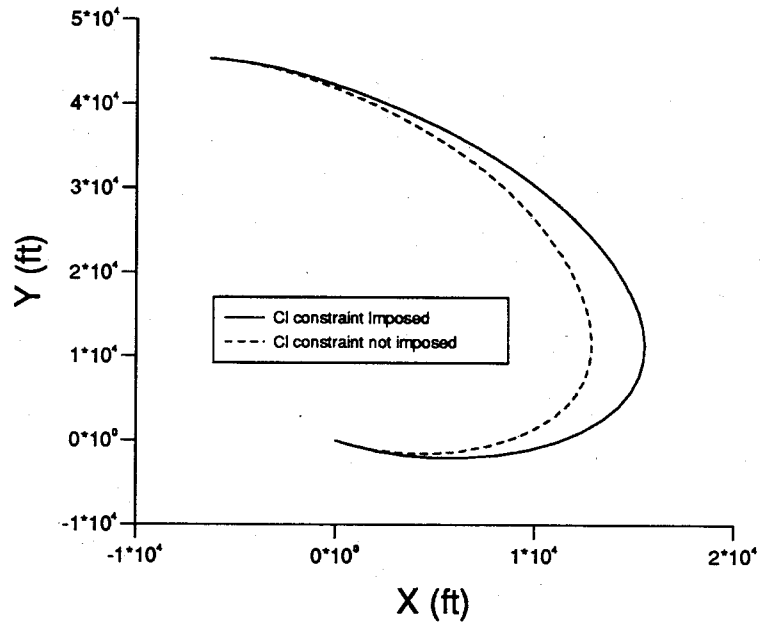


Figure 31: Groundtrack for RTLS Abort at 30 Seconds: Effect of C_L Constraint

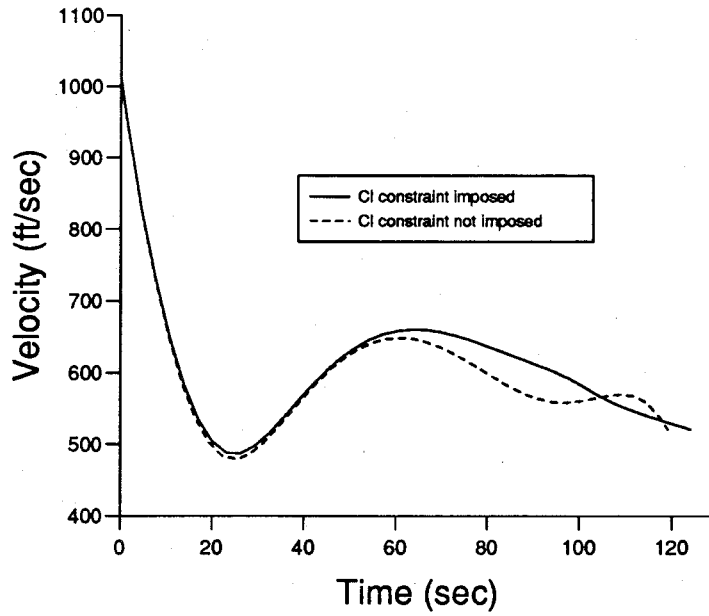


Figure 32: Velocity vs. Time for RTLS Abort at 30 Seconds: Effect of C_L Constraint

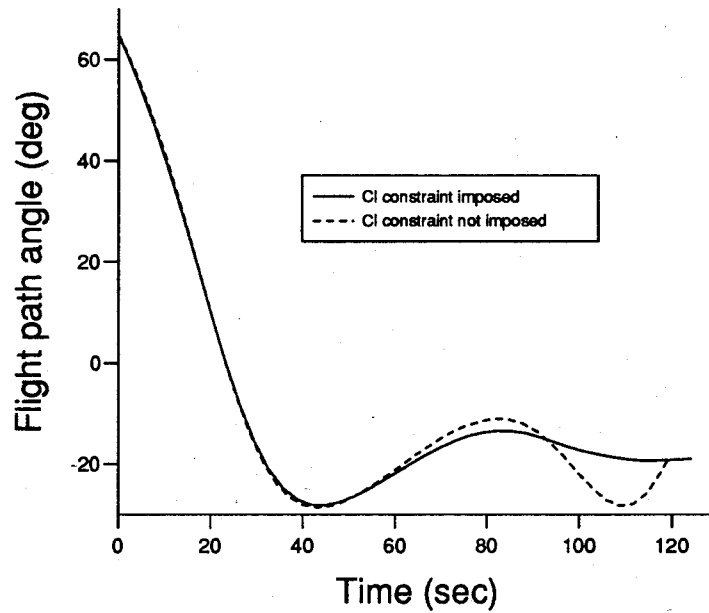


Figure 33: Flight Path Angle vs. Time for RTLS Abort at 30 Seconds: Effect of C_L Constraint

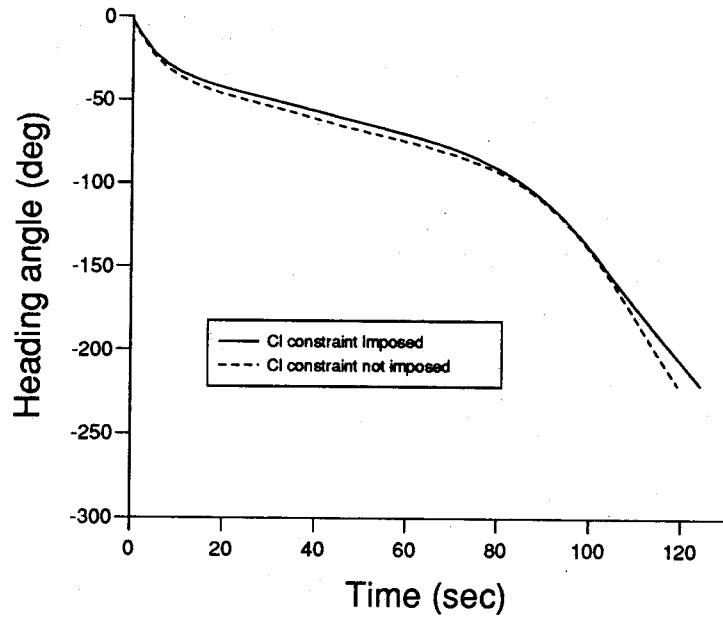


Figure 34: Heading vs. Time for RTLS Abort at 30 Seconds: Effect of C_L Constraint

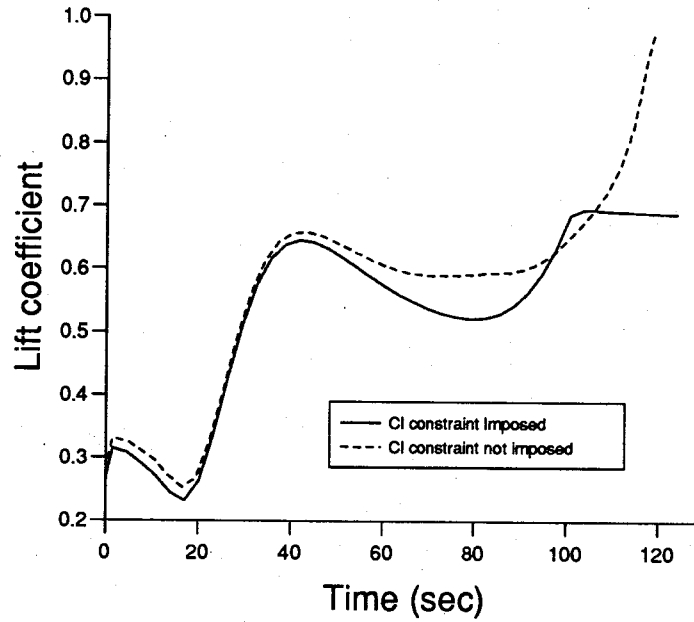


Figure 35: Lift Coefficient vs. Time for RTLS Abort at 30 Seconds: Effect of C_L Constraint

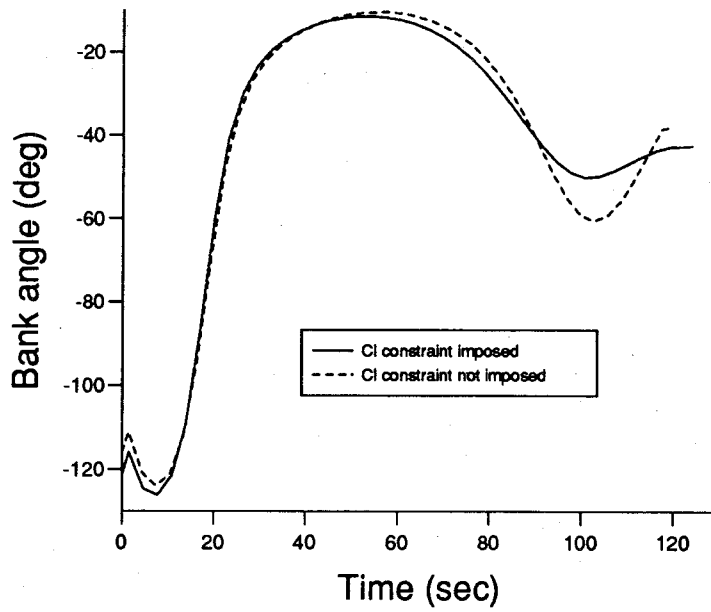


Figure 36: Bank Angle vs. Time for RTLS Abort at 30 Seconds: Effect of C_L Constraint

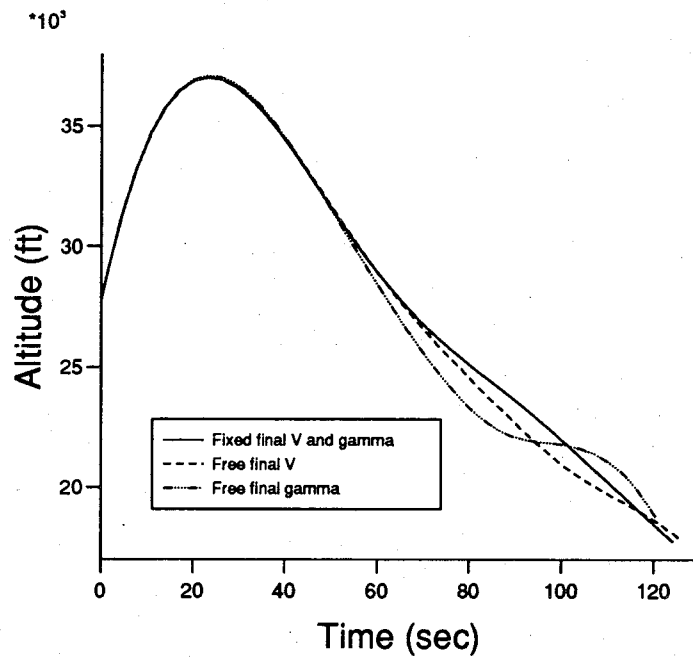


Figure 37: Altitude vs. Time for RTLS Abort at 30 Seconds: Effect of Free Final Boundary Conditions

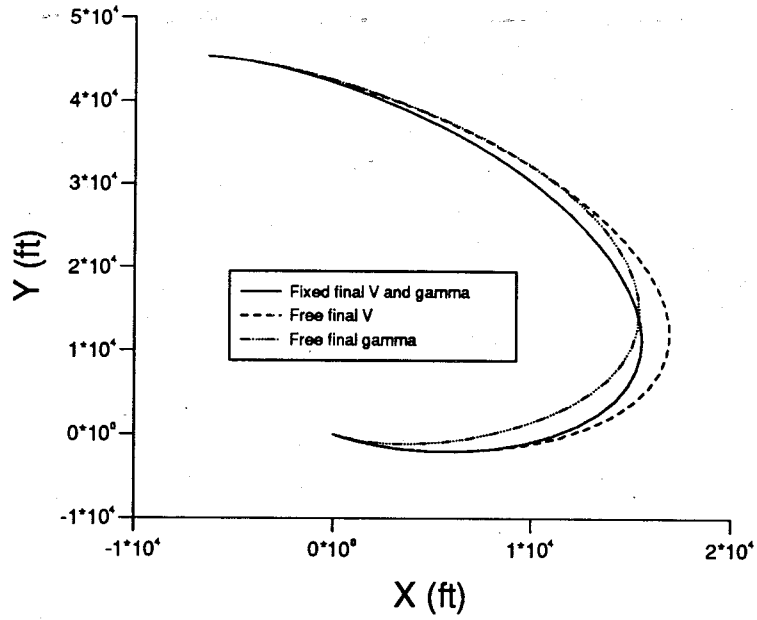


Figure 38: Groundtrack for RTLS Abort at 30 Seconds: Effect of Free Final Boundary Conditions

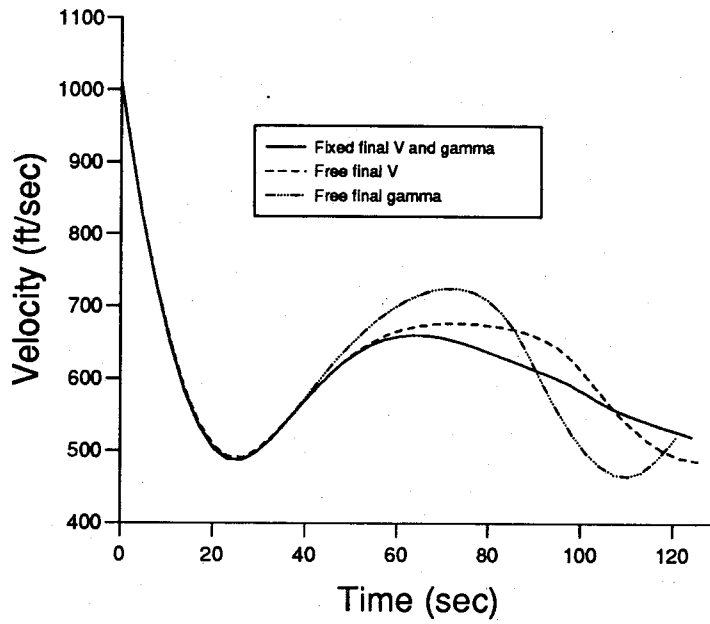


Figure 39: Velocity vs. Time for RTLS Abort at 30 Seconds: Effect of Free Final Boundary Conditions

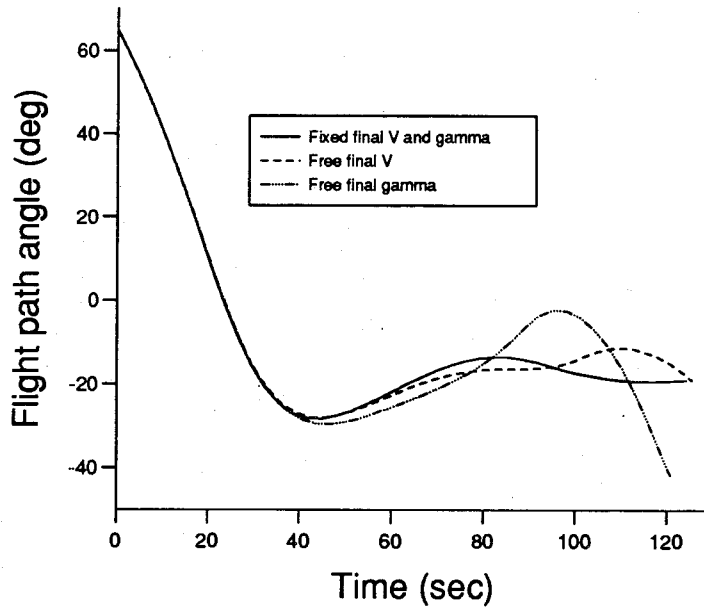


Figure 40: Flight Path Angle vs. Time for RTLS Abort at 30 Seconds: Effect of Free Final Boundary Conditions

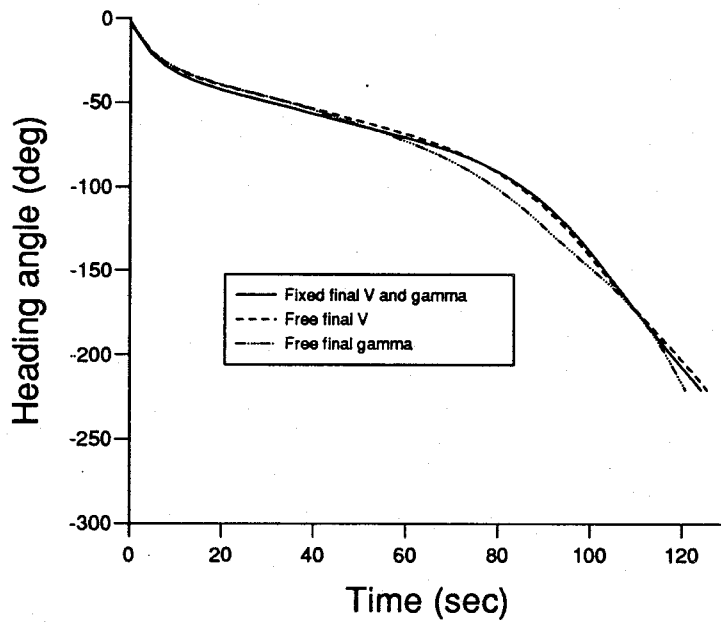


Figure 41: Heading vs. Time for RTLS Abort at 30 Seconds: Effect of Free Final Boundary Conditions

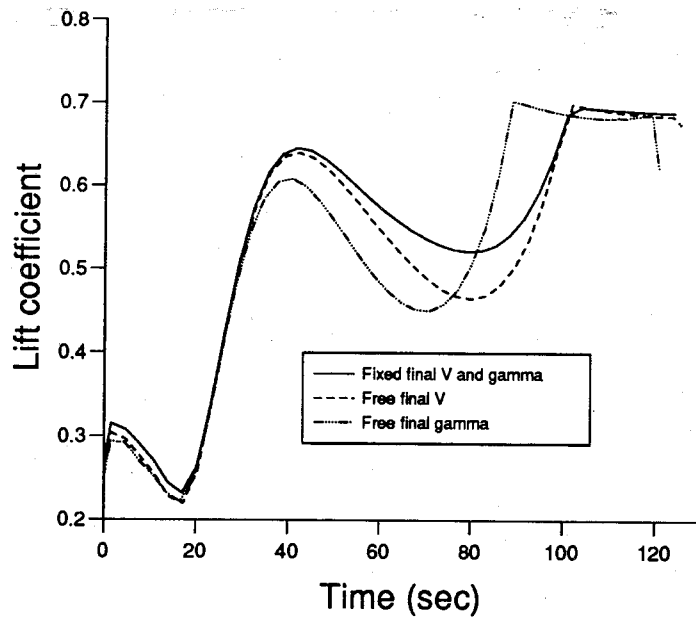


Figure 42: Lift Coefficient vs. Time for RTLS Abort at 30 Seconds: Effect of Free Final Boundary Conditions

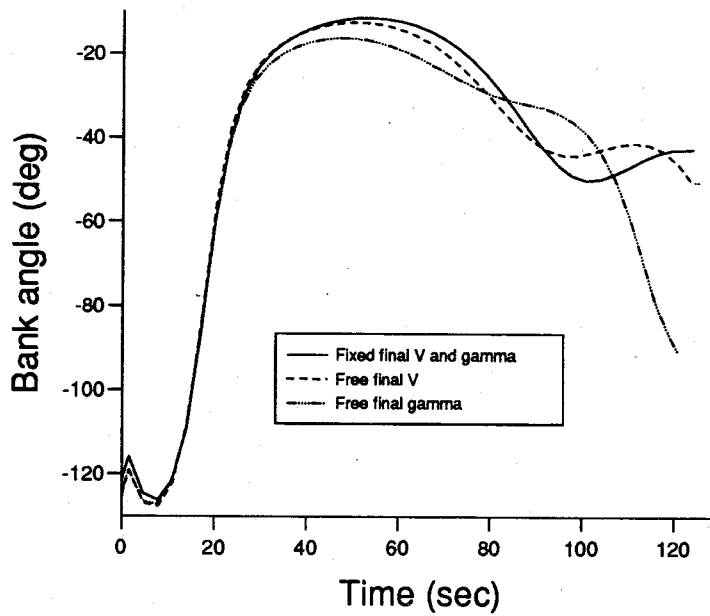


Figure 43: Bank Angle vs. Time for RTLS Abort at 30 Seconds: Effect of Free Final Boundary Conditions

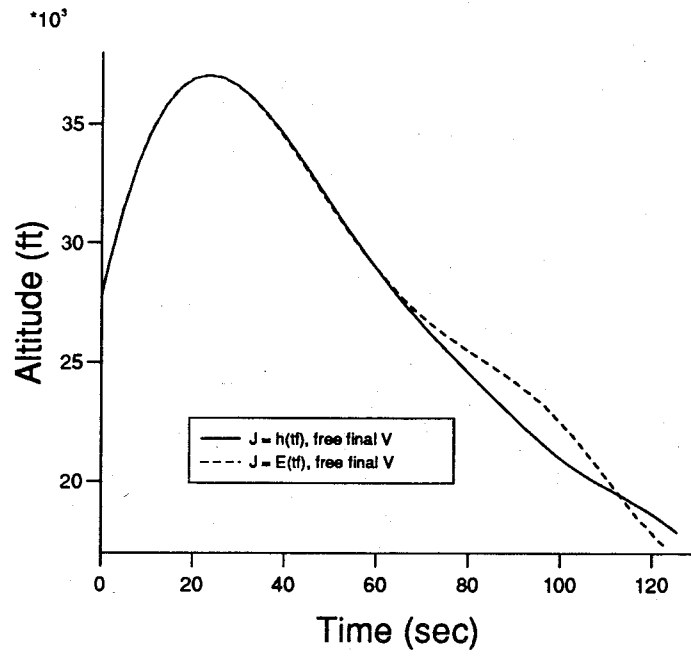


Figure 44: Altitude vs. Time for RTLS Abort at 30 Seconds: Effect of Final Energy as Cost Function

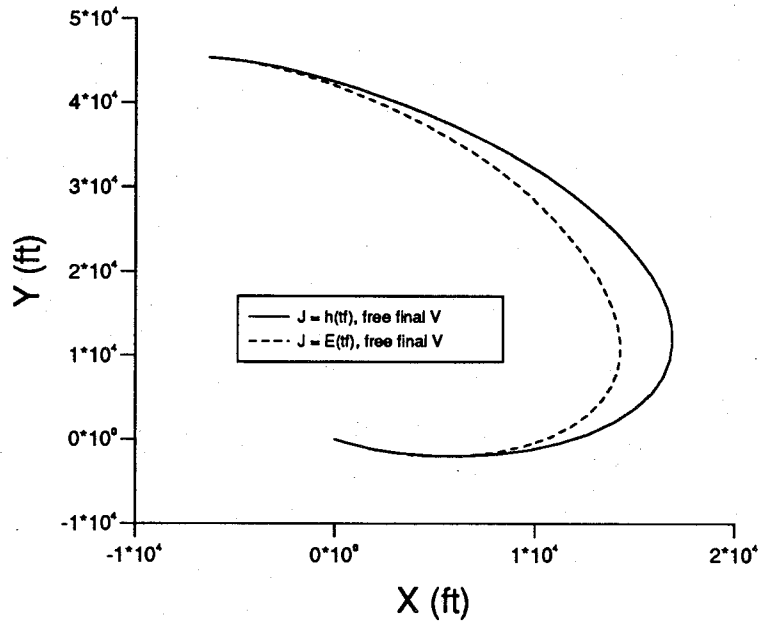


Figure 45: Groundtrack for RTLS Abort at 30 Seconds: Effect of Final Energy as Cost Function

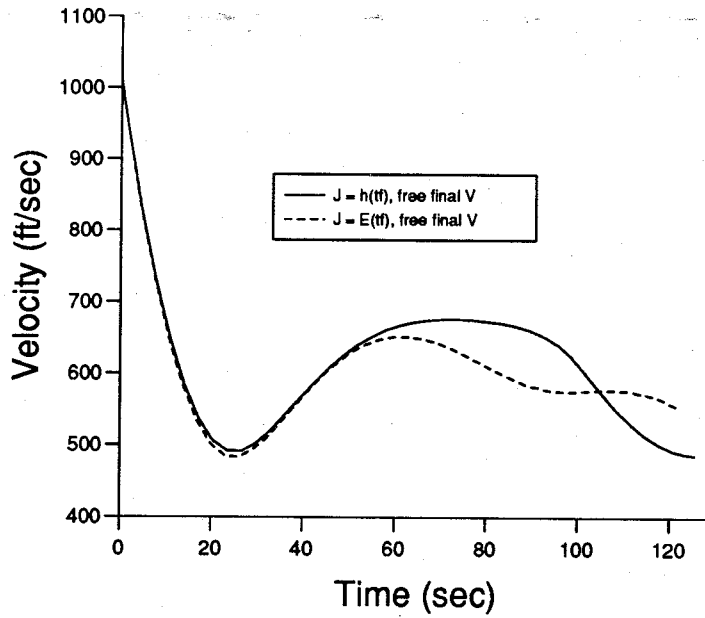


Figure 46: Velocity vs. Time for RTLS Abort at 30 Seconds: Effect of Final Energy as Cost Function

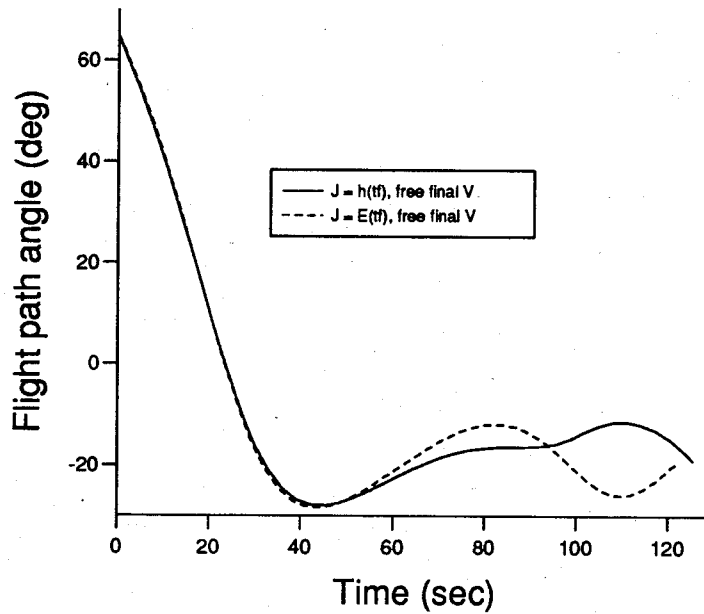


Figure 47: Flight Path Angle vs. Time for RTLS Abort at 30 Seconds: Effect of Final Energy as Cost Function

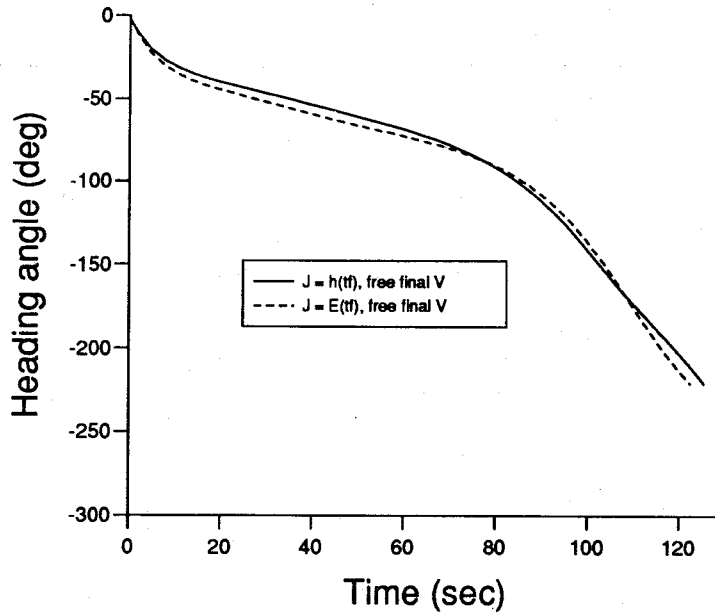


Figure 48: Heading vs. Time for RTLS Abort at 30 Seconds: Effect of Final Energy as Cost Function

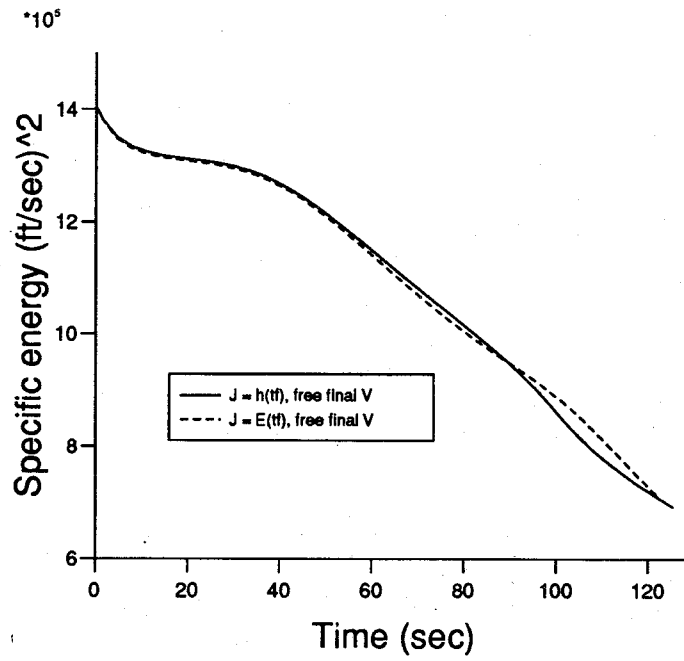


Figure 49: Energy vs. Time for RTLS Abort at 30 Seconds: Effect of Final Energy as Cost Function

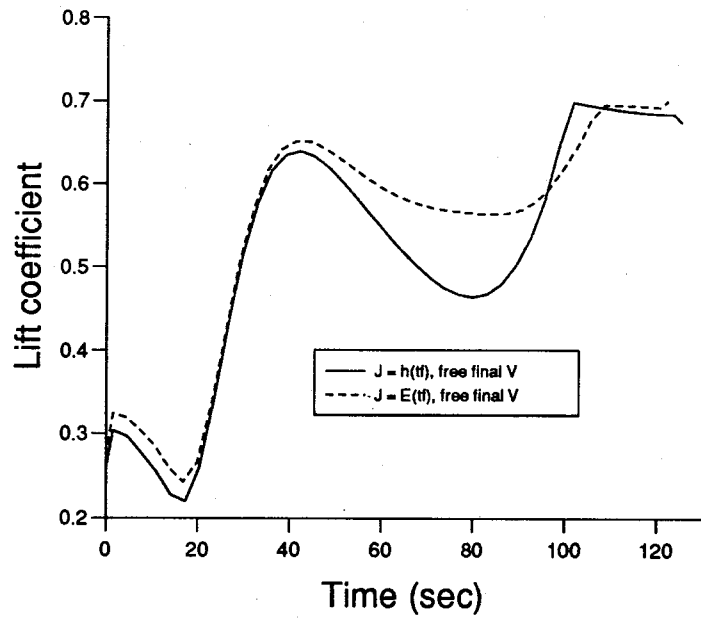


Figure 50: Lift Coefficient vs. Time for RTLS Abort at 30 Seconds: Effect of Final Energy as Cost Function

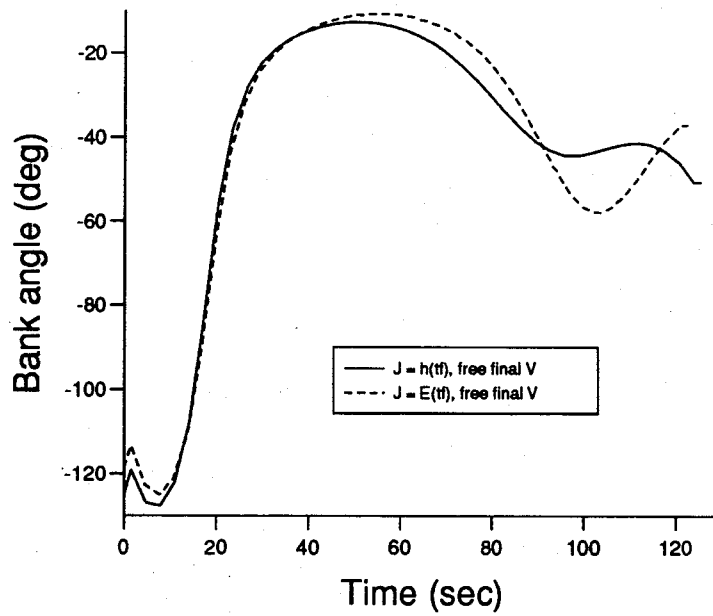


Figure 51: Bank Angle vs. Time for RTLS Abort at 30 Seconds: Effect of Final Energy as Cost Function

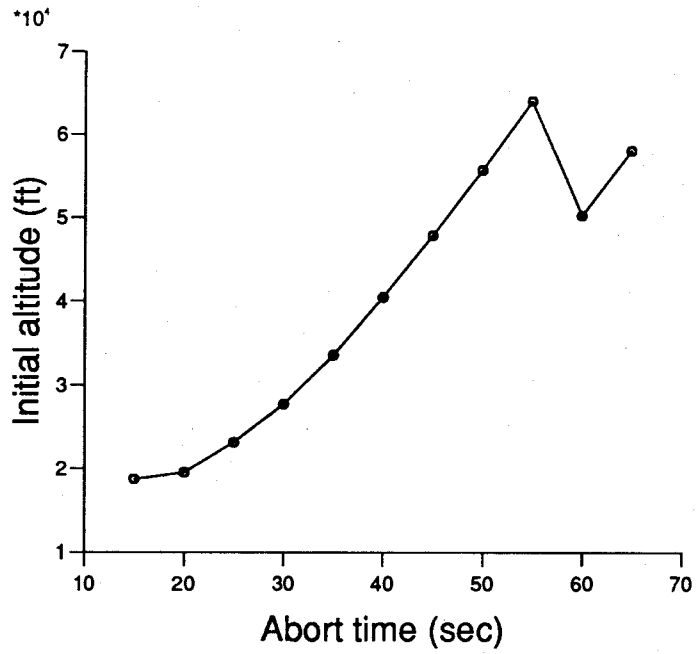


Figure 52: Initial Altitude for HL-20 RTLS Abort

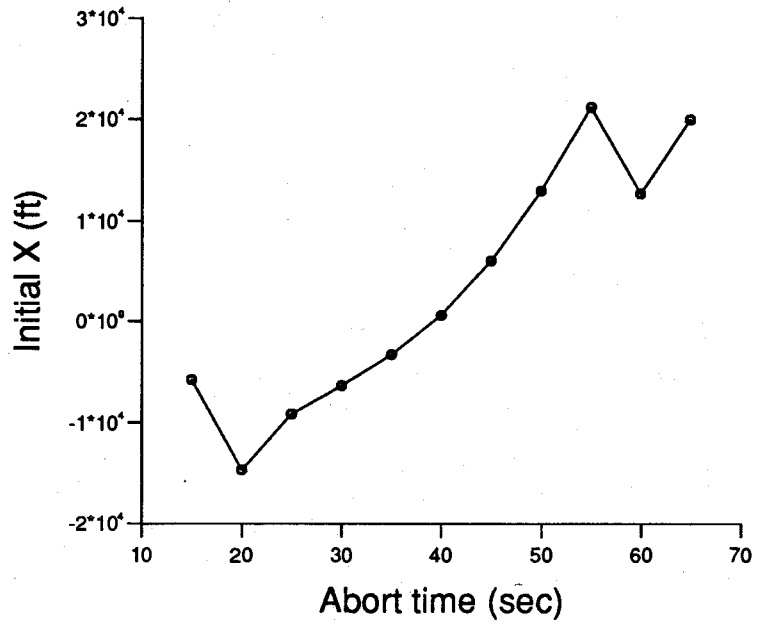


Figure 53: Initial X for HL-20 RTLS Abort

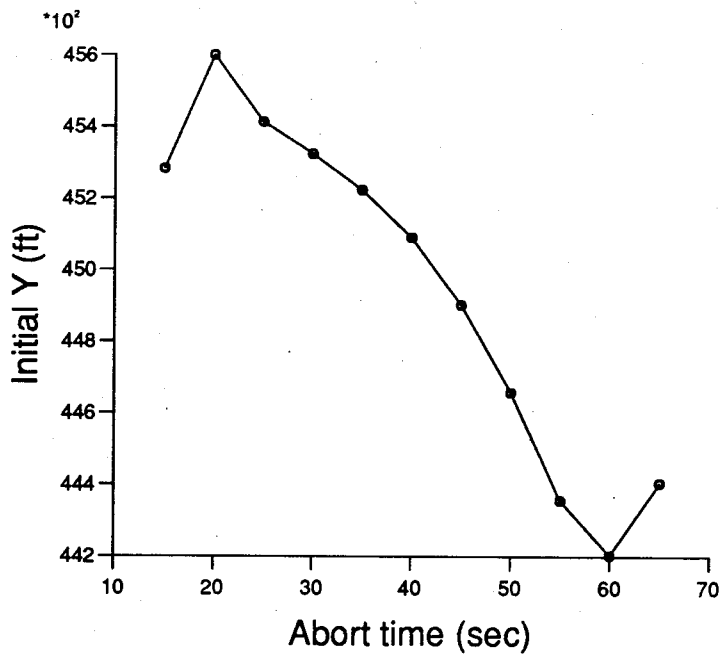


Figure 54: Initial Y for HL-20 RTLS Abort

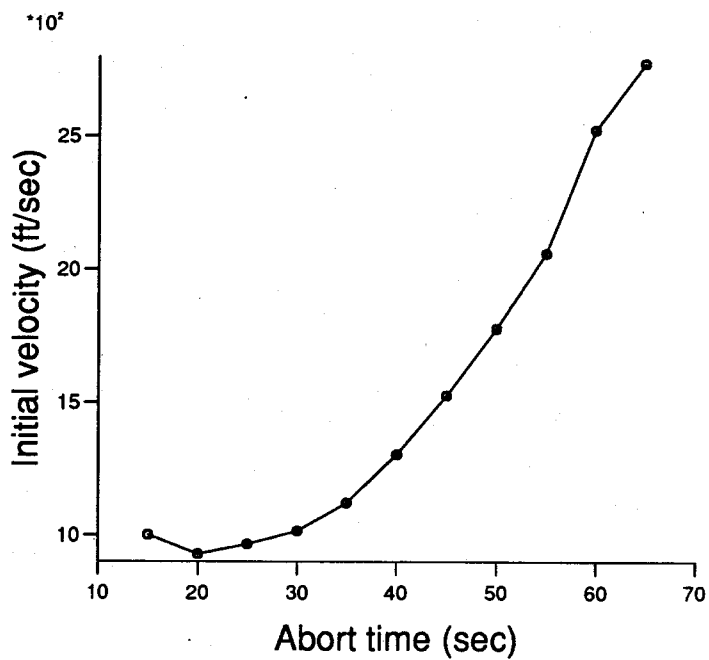


Figure 55: Initial Velocity for HL-20 RTLS Abort

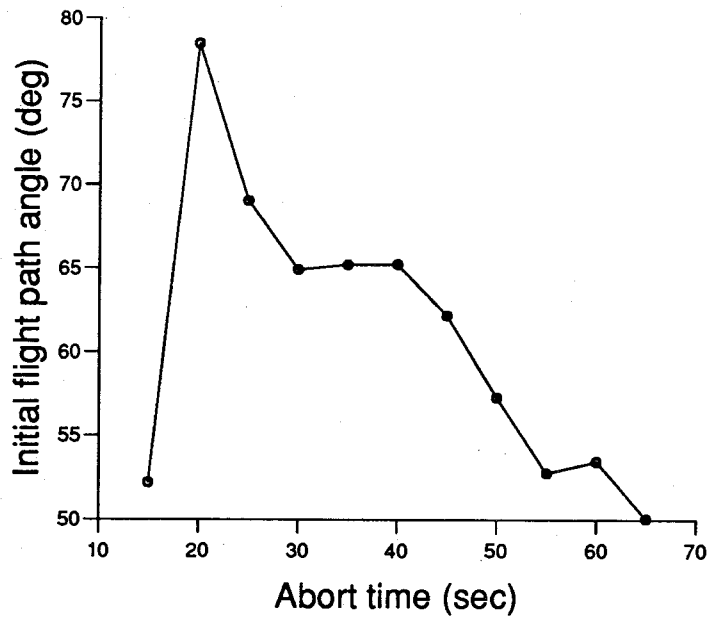


Figure 56: Initial Flight Path Angle for HL-20 RTLS Abort

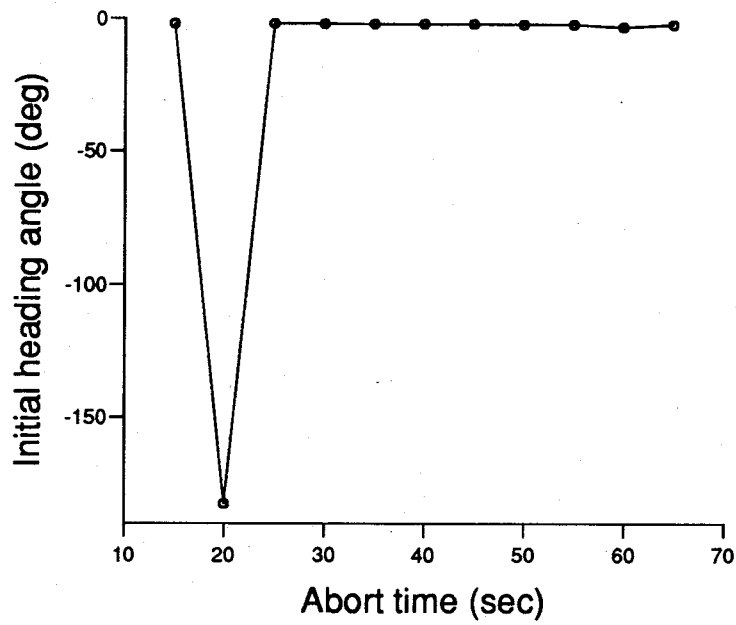


Figure 57: Initial Heading for HL-20 RTLS Abort

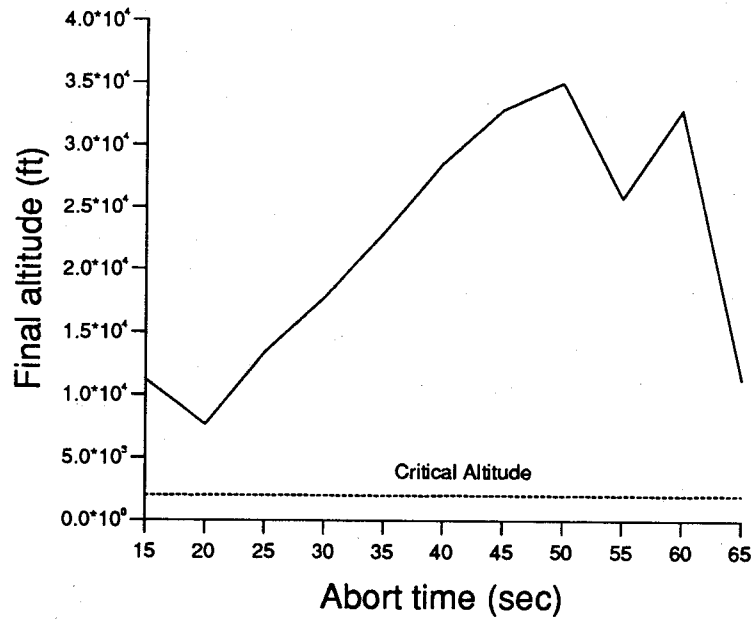


Figure 58: Cost Function vs. Abort Time

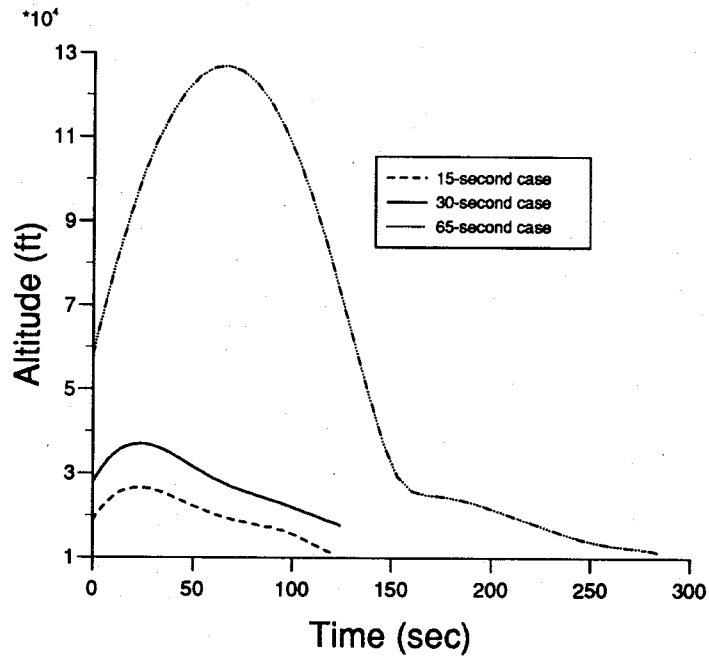


Figure 59: Altitude vs. Time for 15-, 30-, and 65-Second Aborts

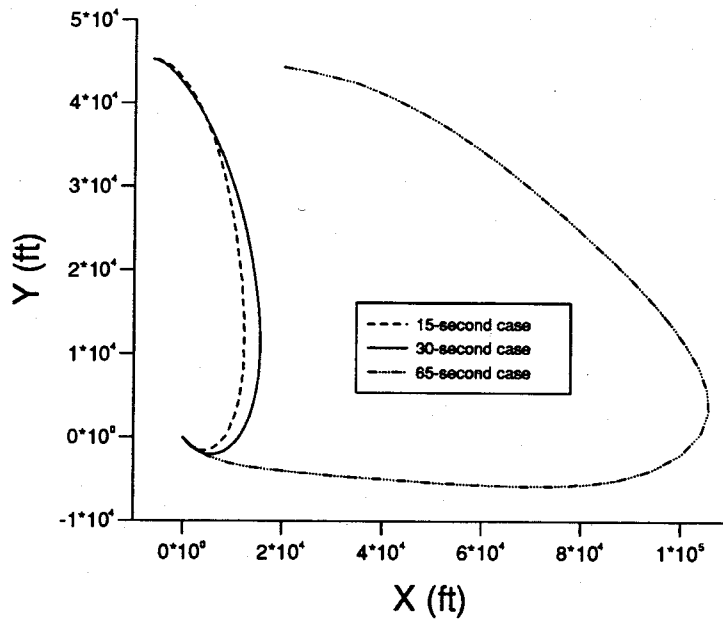


Figure 60: Groundtrack for 15-, 30-, and 65-Second Aborts

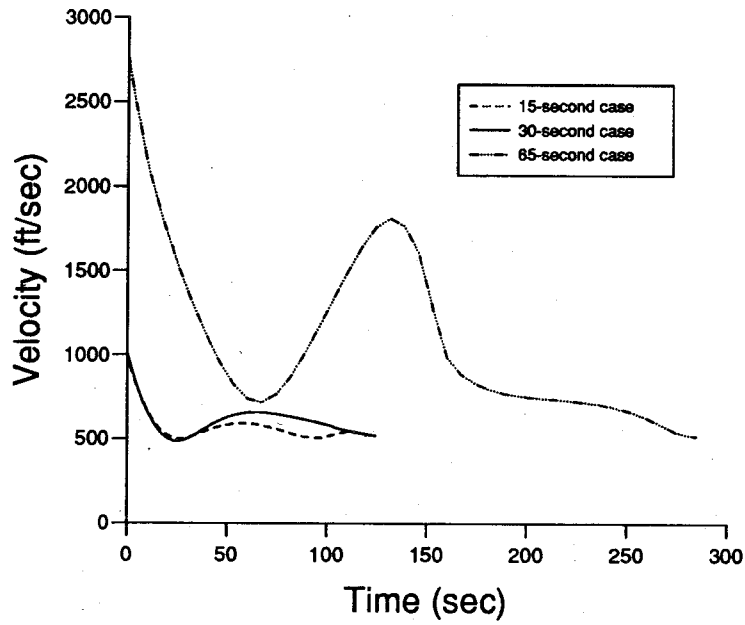


Figure 61: Velocity vs. Time for 15-, 30-, and 65-Second Aborts

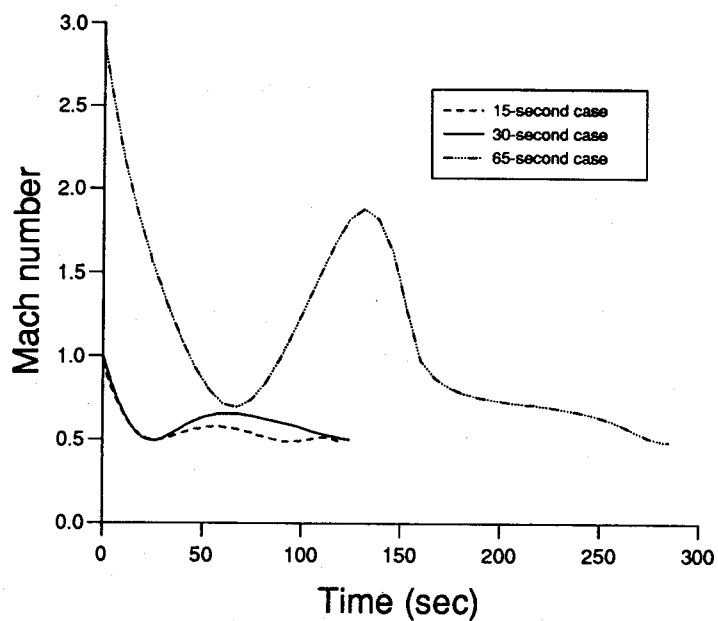


Figure 62: Mach Number vs. Time for 15-, 30-, and 65-Second Aborts

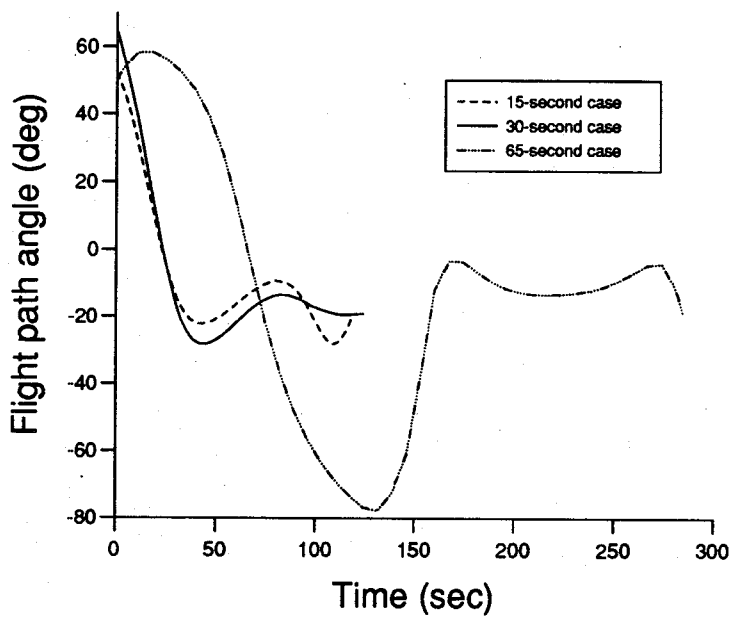


Figure 63: Flight Path Angle vs. Time for 15-, 30-, and 65-Second Aborts

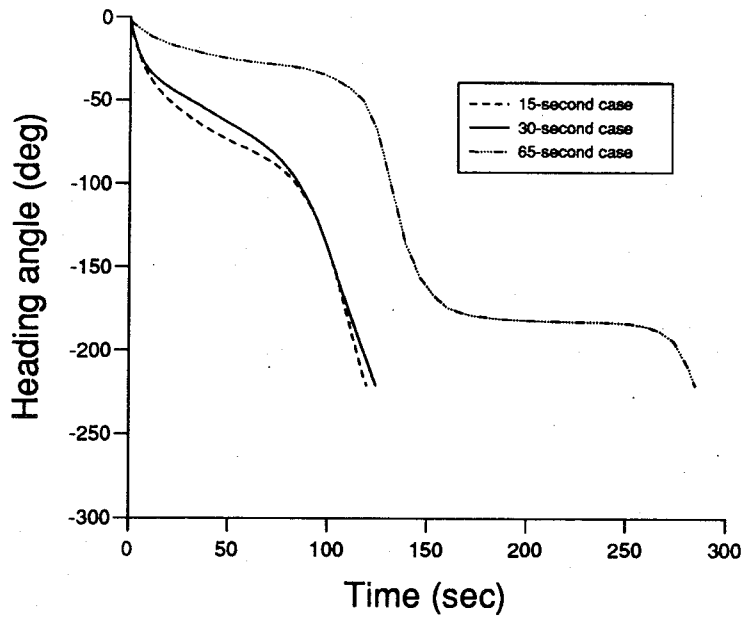


Figure 64: Heading vs. Time for 15-, 30-, and 65-Second Aborts

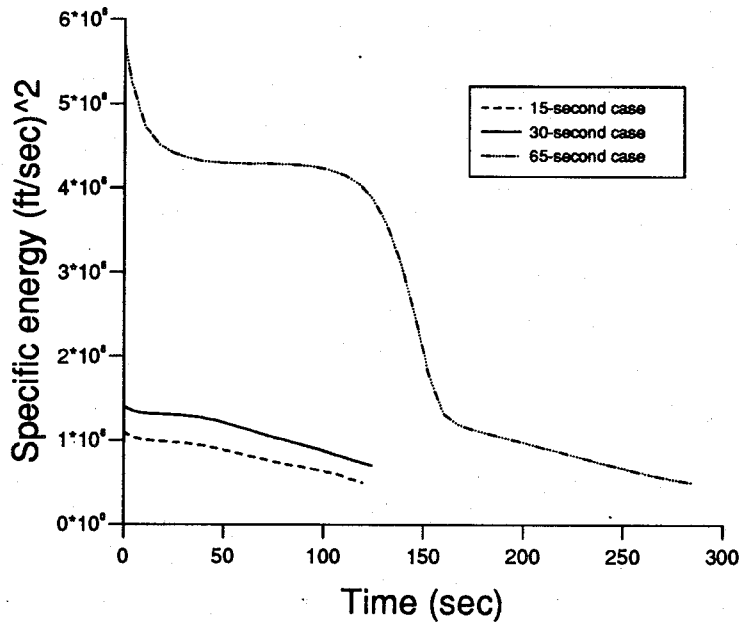


Figure 65: Energy vs. Time for 15-, 30-, and 65-Second Aborts

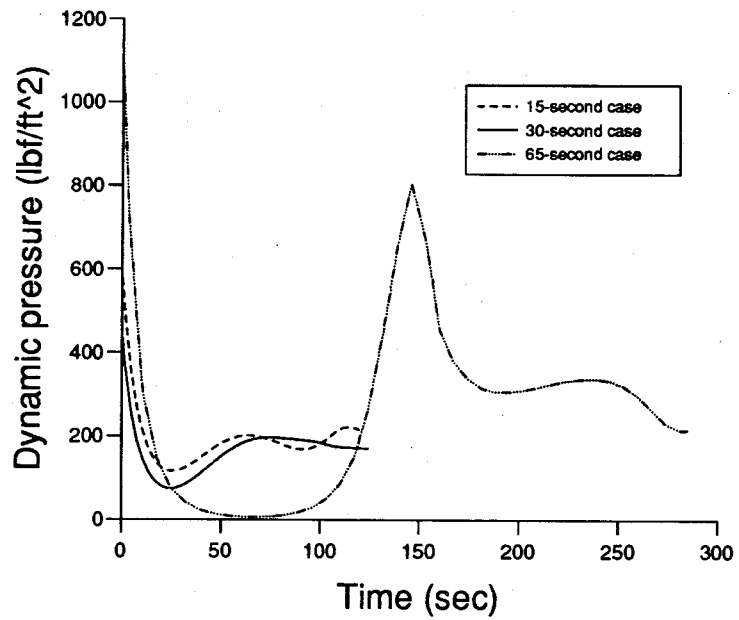


Figure 66: Dynamic Pressure vs. Time for 15-, 30-, and 65-Second Aborts

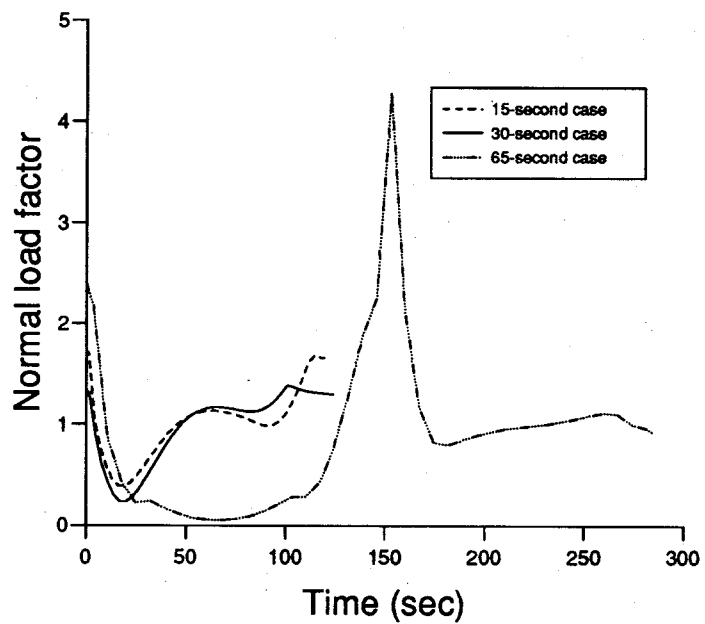


Figure 67: Normal Load Factor vs. Time for 15-, 30-, and 65-Second Aborts

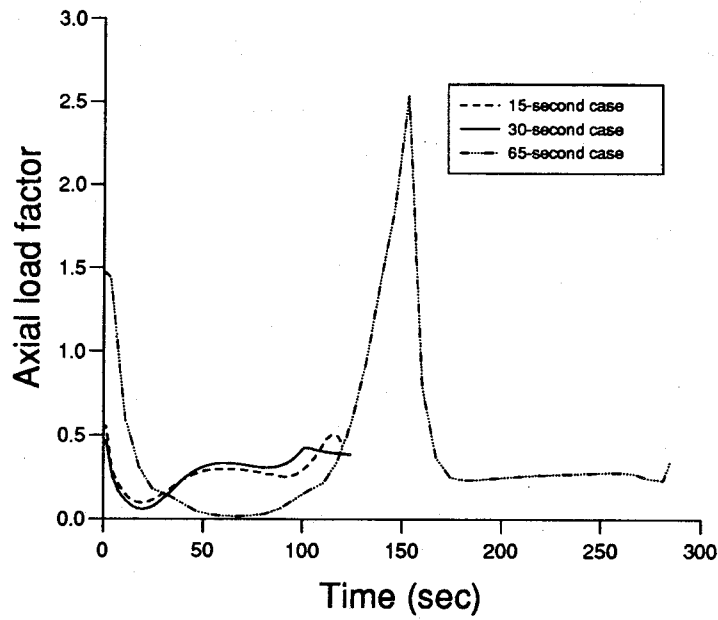


Figure 68: Axial Load Factor vs. Time for 15-, 30-, and 65-Second Aborts

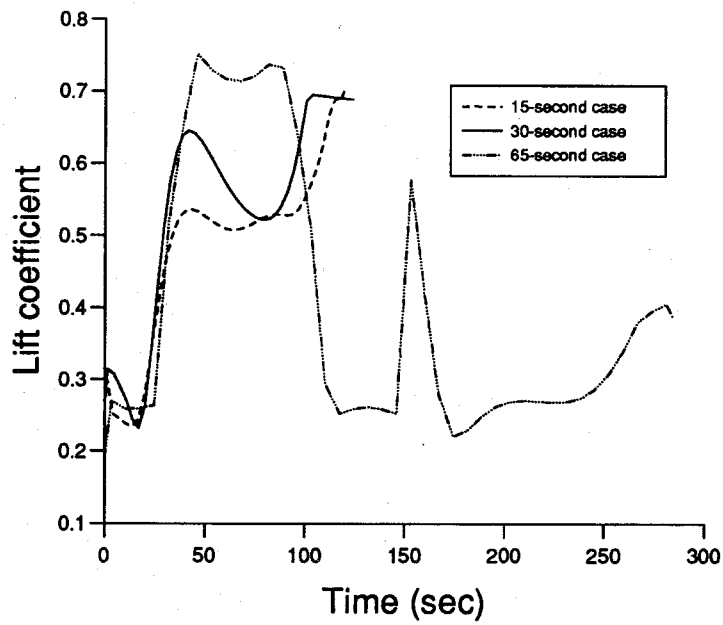


Figure 69: Lift Coefficient vs. Time for 15-, 30-, and 65-Second Aborts

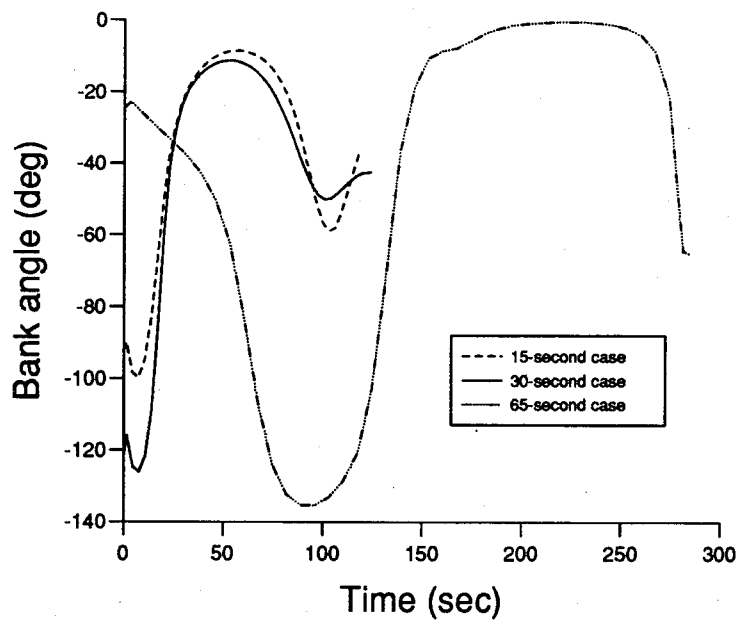


Figure 70: Bank Angle vs. Time for 15-, 30-, and 65-Second Aborts